From the University Clinic for Cardiac and Thoracic Surgery

Medical Faculty

Otto-von-Guericke University, Magdeburg

ESTABLISHMENT OF A THREE-DIMENSIONAL (3D) LUNG CANCER MODEL FOR TRANSLATIONAL RESEARCH

D I S S E R T A T I O N

Submitted for the degree

Dr. med.

(doctor medicine)

at the Medical Faculty

Otto-von-Guericke University, Magdeburg

Submitted by: Hailong Wang

From: Shandong, China

Magdeburg   2023

Zusammenfassung:

In der Vergangenheit wurden verschiedene sphäroidische, organotypische und dreidimensionale (3D) Bioprinting-Lungenkrebsmodelle für in-vitro-Wirkstofftests und die personalisierte Medizin entwickelt. Diese Gewebemodelle können die Mikroumgebung des Lungentumors (TME) nicht abbilden, weshalb die Forschung zu den Interaktionen zwischen Tumorzellen und TME begrenzt ist. Um diese Hürde zu überwinden, haben wir von Patienten stammende Lungentumorproben verwendet, um neue In-vitro-3D-Modelle unter drei verschiedenen Kulturbedingungen zu etablieren: statisch, dynamisch und Co-Kultivierung. Alle drei Kulturbedingungen ermöglichten eine Gewebekultur von bis zu 28 Tagen. Die Erfolgsrate des statischen 3D-Lungenkrebsmodells war deutlich höher als die des entsprechenden 2D-Modells. Unsere Gewebemodelle wurden durch Hämatoxylin-Eosin-Färbung und Immunfluoreszenzfärbung charakterisiert. Wir fanden Tumorzellen, die positiv für spezifische Lungenkrebsmarker (TTF-1 und p40/p63) waren, krebsassoziierte Fibroblasten (CAFs), die positiv für α-SMA und MCT4 waren, und extrazelluläre Matrix für Fibronektin (FN). Mittels DAPI-Färbung bestimmten wir die Zelldichte des statischen 3D-Modells, die von Tag 21 bis Tag 28 zunahm. Die mit dem M30-ELISA gemessene Apoptose nahm von Tag 21 bis Tag 28 ab. 3D-Modelle, die mit NIH-3T3-Zellen kultiviert wurden, wiesen jedoch im Allgemeinen eine geringere Apoptose auf. Außerdem führten wir erste Tests durch, bei denen wir die Zellen auf der SISmuc-Matrix als Ersatzmaterial für unser 3D-Modell kultivierten. Insgesamt wurde ein neuartiges in vitro 3D-Lungenkrebsmodell erstellt, das das TME für 28 Tage simulierte und eine strukturelle Komplexität besaß.

Bibliographic description:

Wang, Hailong:

Establishment of a three-dimensional (3D) lung cancer model for translational research. -2023. 92 pages, 18 figures, 16 tables.

Abstract

In the past, different spheroid-, organotypic-, and three-dimensional (3D) bioprinting lung cancer models were established for *in vitro* drug testing and personalized medicine. These tissue models cannot depict the tumor microenvironment (TME) and therefore research addressing tumor cell-TME interactions is limited. To overcome this hurdle, we applied patient-derived lung tumor samples to establish new *in vitro* 3D models with three different culture conditions: static, dynamic, and co-cultivation. All three culture conditions afforded tissue culture for up to 28 days. The success rates of the static 3D lung cancer model was significantly higher than the corresponding 2D model. Our tissue models were characterized by hematoxylin eosin staining and immunofluorescence staining. We found tumor cells that were positive for specific lung cancer markers (TTF-1 and p40/p63), cancer associated fibroblasts (CAFs) positive for α-SMA and MCT4, and extracellular matrix for fibronectin (FN). Using DAPI staining, we determined the cell density of the static 3D model which increased from day 21 to day 28. Apoptosis measured through the M30 ELISA decreased from day 21 to day 28. 3D models which were co-cultured with NIH-3T3 cells, however, showed lower apoptosis in general. In addition, we performed preliminary tests culturing the cells on the SISmuc matrix for replacement materials of our 3D model. Taken together, a novel *in vitro* 3D lung cancer model was established, which simulated the TME for 28 days and possessed a structural complexity.

Keywords

Non-small cell lung cancer, 3D culture, dynamic culture, primary tissue, tumor microenvironment

Directory

V

Abbreviations

2D	Two-dimensional
3D	Three-dimensional
ADC	Adenocarcinoma
CAFs	Cancer associated fibroblasts
Cck18	Caspase-cleaved keratin 18
ECM	Extracellular matrix
EMT	Epithelial-mesenchymal transition
FN	Fibronectin
hbFb	Human bronchial fibroblasts
NDS	Normal donkey serum
NGS	Normal goat serum
NIH-3T3	Mouse Swiss NIH embryo fibroblasts cell line
NSCLC	Non-small cell lung cancer
OS	Overall survival
PD-L1	Programmed cell death ligand 1
PDO	Patent-derived organoid
PDX	Patient-derived xenograft
ROCK	Rho kinase
RT	Room temperature
SCLC	Small cell lung cancer
SIS	Small intestinal submucosa
SQCC	Squamous cell lung cancer
TAMs	Tumor associated macrophages
TME	Tumor microenvironment

List of Figures

List of Tables

1. Introduction

1.1. Lung Cancer

1.1.1. Epidemiology of Lung Cancer

Lung cancer is the leading cause of cancer-related death worldwide, with a 5-year survival rate of only 26% for non-small cell lung cancer (NSCLC) (American Cancer Society, 2020). In Germany, the incidence rates of lung cancer are 32.7 and 52.1 (per100,000) in women and men, respectively, and it is the third cancer in women and second cancer in men of all newly diagnosed cancers accounting for 9.4% and 13.3%, respectively (Koch, 2018). In China, there were 787 000 new lung cancer cases (520 000 men and 267 000 women) with a morbidity rate of 57.26 per 100 000 population, and 631 000 lung cancer deaths with a mortality rate of 45.87 per 100 000 population (Zheng et al., 2019). Among several risk factors, smoking is regarded as the most common reason for lung cancer and the prevention strategies are focusing on reducing the long-term smoking habits in adolescents. Following the strict policies of advertising and broad information campaigns, the smoking incidence in adolescents decreased from 28% in 2001 to 7% in 2018 (Frost et al., 2022).

1.1.2. Classification of Lung Cancer

According to the pathological classification, lung cancer is generally separated into two groups, small cell lung cancer (SCLC) and non-small cell lung cancer (NSCLC). The SCLC is fast-paced, from neuroendocrine (NE) cell origin, and a mostly lethal lung cancer. Patients with SCLC have a low 5 year survival rate of 7% (FreseSimpson & Dive, 2021). NSLCL is distinguished into three main subtypes: squamous cell lung cancer (SQCC), adenocarcinoma (ADC) and large cell carcinoma according to their cellular origin. The morphology and immune staining play an important role in the diagnosis of lung cancer. All

current clinical trial data that justify the importance of the distinction between histological types of NSCLC in advanced lung cancer patients are based on light microscopy with or without mucin stains but not on the basis of immunohistochemical stains (Travis et al., 2013). The majority of SQCC and ADC (56%) can be identified with cytomorphology alone (Kimbrell, Gustafson, Huang, & Ehya, 2012) and 38% of the samples can be identified with extra immune staining (Zakowski et al., 2016). The most common used lung cancer markers are TTF-1 for adenocarcinoma and p63/p40 for squamous cell lung cancer. TTF-1 (Nkx2.1) is a member of the Nkx2 family of transcription factors, which is the predominant marker utilized for identifying neoplasm of lung origin and it has a sensitivity ranging from 75% to 80% for lung ADC (BishopSharma & Illei, 2010; Gurda et al., 2015). The expression of TTF-1 is also correlated with the degree of tumor differentiation, i.e. high differentiated ADCs are more likely to express TTF-1 compared to poor differentiated tumors (Rekhtman, Ang, Sima, Travis, & Moreira, 2011). P40 and P63 are products of the P63 gene on chromosome 3q27–29, and basal or progenitor cell layer of bronchial epithelium express both of them (Lilo et al., 2016).

1.1.3. Treatment of Lung Cancer

Surgical treatment is commonly selected for patients with early stage of NSCLC (DumaSantana-Davila & Molina, 2019). As for the advanced stage NSCLC patients, multidisciplinary team (MDT) are considered to achieve an optimal treatment for patients (Evison, 2020). In recent years, immune therapy with the immune checkpoint inhibitors (ICIs) has influenced the landscape of NSCLC treatment (GuoBai & Cui, 2020). Around 40% of patients with NSCLC mutation were recommended to chose targeted therapy in Germany. Patients without NSCLC mutation may receive immune checkpoint inhibitor treatment according to their PD-L1 status (Frost et al., 2022). In addition, anti-angiogenesis therapy has been proven to prolong the first endpoint of

overall survival (OS) and second endpoint of progression-free survival (PFS) (WuWang & Zhou, 2021).

1.2. *In Vivo* and *In Vitro* Models of Lung Cancer

In order to test different therapies of lung cancer in the clinic, scientists investigated numerous preclinical models of lung cancer, including *in vivo* and *in vitro* models. The most common *in vivo* models are patient-derived xenografts (PDX), xenografts that are derived from patient-derived organoids (PDO-x) and genetically engineered mouse models (GEMM). The *in vitro* lung cancer models include two-dimensional lung cancer cell cultures (2D-LC), lung cancer cell lines, air-liquid interface models, patient-derived organoids (PDO), patient-derived organoid co-cultures (PDO+), xenograft-derived organoids (XDO), and three-dimensional (3D) printing models (Herreros-Pomares et al., 2021; JiaLiang & Li, 2020; Pham et al., 2021). Among these models, the *in vitro* models developed quickly in recent years due to the effective production and controllable cultivation conditions. In addition, the *in vitro* models avoid using animal models and most of them cultured in well plates which saved cultivation materials and space, while the PDX models were resource-intensive and required long time cultivation (Dong et al., 2010; Siolas & Hannon, 2013). In drug testing research, organoid models could be passaged into 384 well plates to adapt the high throughput studies, which greatly improved testing efficiency (Du Y et al., 2020).

1.2.1. 2D Models

Cell lines were designed as *in vitro* 2D models due to the stable genetic expression and various mutation types. Meanwhile, the patient-derived cell lines represent the genetic diversity both in transcriptional profile and the phenotypic properties of primary lung cancer cells. With these diverse cell lines, scientists could validate the drug activity mechanisms from genomics,

phenotypes, and functionality. For example, EGFR mutations were investigated to be the strongest predictor of sensitivity of EGFR inhibitor Erlotinib through the established 2D models (Sos et al., 2009). KH-type splicing regulatory protein was identified as a metastasis-associated candidate molecule in five different NSCLC cell lines (Yan et al., 2019). The knockdown of this gene could inhibit the proliferation, increase the apoptosis, and lead to cell-cycle arrest in A549 cells (Ge et al., 2019).

After cluster analysis, Shen and other colleagues compared three adenocarcinoma lung cancer samples from The Cancer Genome Atlas (TCGA) and seven cell lines from The Genomics of Drug Sensitivity in Cancer (GDSC) database with the same second cluster. They found that all cell lines had high IC_{50} value and showed marked pharmacological resistance to Cisplatin, while only three tumor samples showed complete response to Cisplatin (Shen, Xiang, Huang, Zhang, & Yue, 2022). Moreover, the high passage and selection of cell lines generate gene mutation which influence the characteristic of the cell line. In one experiment, the selected invasive lung cancer cell line (A549-I5) significantly expressed 83 different proteins compared to the common lung cancer cell line (A549). These proteins were considered to be associated with metastasis of lung cancer due to their epithelial-mesenchymal transition (EMT) functions (Kuo et al., 2021). Although 2D models work as a convenient tool for the investigation of lung cancer, the inconsistent results between cell lines and actual tumor samples underscore the shortcomings of cell lines.

1.2.2. Organoids

Although numerous cell lines of lung cancer could afford the therapy screening, the clinical trials reflected diverse results based on this research. In US-studies, 95% of the new lung cancer drug candidates failed in the final clinical trials (Kaczmarczyk et al., 2021). Such a high attention forced scientists to

4

investigate three dimensional models, which could mimic the native outgrowth of lung cancer cells *ex vivo*. The organoid technology provides a new method for *in vitro* cultivation which has better key histological and molecular traits of their parental tumors than cell lines (Broutier et al., 2017). In the group of Shi, they described a method to generate short-term within three month and long-term with more than three month of NSCLC organoids. Each passage could be kept no longer than four weeks (Shi et al., 2020). The lung adenocarcinoma is more likely to generate organoids compared to squamous cell lung cancer, which is as difficult as the generation of 2D cell line from squamous cell lung cancer. In addition, it also has a higher success rate to generate lung cancer organoid from xenograft than the patient tumor, which suggested a prior selection pressure of xenograft enriched tumor cells (John et al., 2011; Wang et al., 2017).

Most of the lung cancer organoids are cultured with the medium formulations used for 2D cell line, which included B-27 and N2 supplements, and growth factors. Some groups added Nutlin-3a, an early type of MDM2 inhibitors, to enrich TP53 mutation tumor cells (Sachs et al., 2019). Because the Nutlin-3a could disturb the p53-MDM2 interaction and lead to reactivation of p53 for the apoptosis, especially in wild type TP53 cells (Konopleva et al., 2020). In addition, a lot of groups add Wnt3a (He et al., 2015) and Noggin (Laurila, Parkkila, Isola, Kallioniemi, & Alarmo, 2013) in the medium. Noggin suppressed the osteoblastic formation of the lesion in bone and the tumor growth *in vivo* with A549 cell line. Wnt3a could induce Wnt signaling pathway which plays an instrumental role in stem cell self-renewal (ArosPantoja & Gomperts, 2021). However, Noggin suppressed the osteoblastic formation of the lesion in bone and the tumor growth *in vivo* with A549 cell line (Feeley et al., 2006).

Due to the high preservation of molecular traits, the PDO models could be used for drug screening and biomarker discovery. With the established chemotherapy docetaxel, which targets cellular micro-tubules, lung cancer

organoids showed lower sensitivity than normal bronchial organoids. However, different chemotherapy, Olaparib and Erlotinib, showed different sensitivity in the lung cancer organoids (Kim et al., 2019). With machine learning and PDO from 41 patient tumors and 5 xenografts, the gene signatures led to classifiers for distinguishing responsive and non-responsive organoids. These classifiers with high sensitivity and specificity were discovered as new biomarkers for drug testing (Schütte et al., 2017).

1.3. Tumor Microenvironment

In the primary tumor site and metastatic site, the tumor microenvironment is influenced and modified with the development of tumor such as tumor initiation, progression, invasion, and colonization in metastatic site. In addition, during the dissemination, tumor cells living in the blood system which is a special tumor microenvironment *in vivo* including platelet, myeloid cells and other blood cells (Figure 1). In the TME of lung cancer, the cellular component consists of four different cell types, including vascular cells, tumor-associated macrophages (TAMs), regulatory T cells (Tregs), tumor-infiltrating lymphocytes (TILs), such as CD4+ and CD8+ T cells, natural killer (NK) cells, stromal cells, such as cancer-associated fibroblasts (CAFs), and dendritic cells (DCs). These cells interact with each other through contact-dependent communication, which is mediated by adherent molecules. The famous example for this is the PD-1/ PD-L1 pathway. Besides this, paracrine signaling is also a critical communication method between tumor cells, host cells, and other stromal cells (de Visser & Joyce, 2023a). In addition, the ECM also plays e.g. a role in determining the dormancy and reawakening of tumor cells (Di Martino et al., 2022). ECM proteins such as tenascin-C (Oskarsson et al., 2011), type I collagen (Barkan et al., 2010) or fibronectin act as pro-metastatic factors, in addition to being structural components of the metastatic niche (Aguirre-Ghiso, Liu, Mignatti, Kovalski, & Ossowski, 2001).
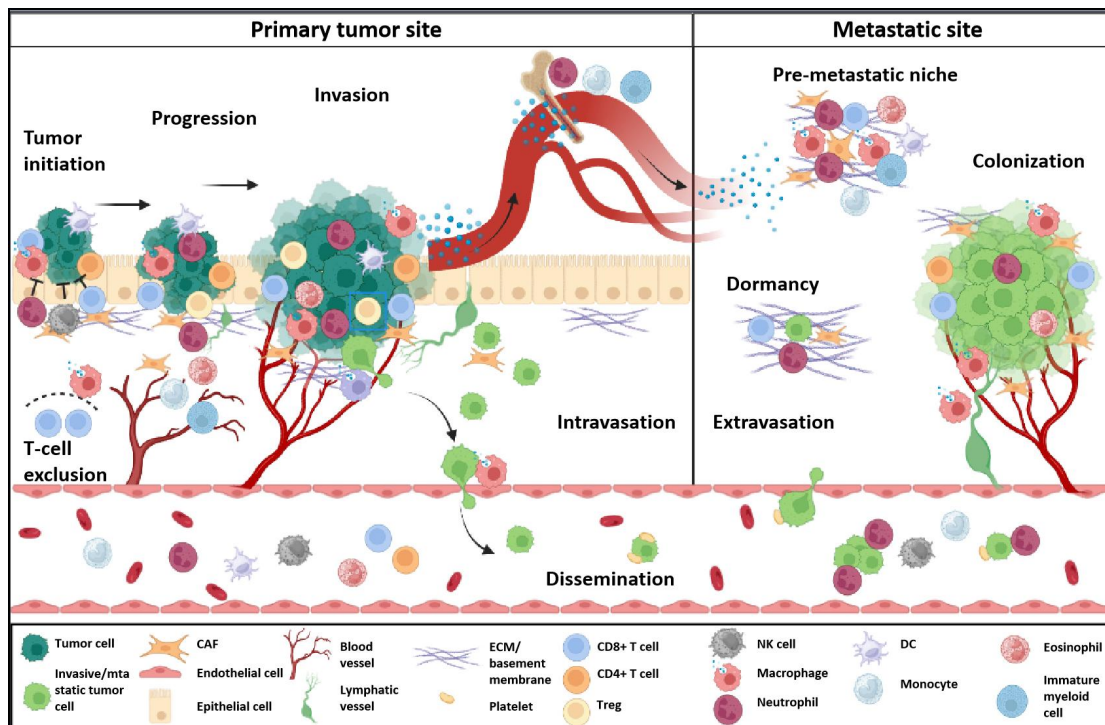
Figure 1. Tumor microenvironment components.

The cellular components of the tumor microenvironment include tumor cells, cancer-associated fibroblast cells, epithelial cells, tumor-associated lymphocytes and macrophages, among others. This figure was created with BioRender.com and modified according to the publication (de Visser & Joyce, 2023b).

1.3.1. CAFs

Tumor cells do not exist in isolation *in vivo*, and carcinogenesis depends on the surrounding tumor microenvironment (TME), which is composed of four main cell types and biophysical and biochemical components. Fibroblasts are essential in maintaining this tissue homeostasis (Chhabra & Weeraratna, 2023). The formation and turnover of tumor ECM are related to fibroblasts producing collagen, fibronectin, laminin, and secreted enzymes, such as lysyl hydroxylases and metalloproteinases, to modify the molecular structures (Lynch & Watt, 2018; Voloshenyuk, Landesman, Khoutorova, Hart, & Gardner, 2011). Among all types, there is a group of fibroblasts that are attracted by the

growth factors secreted by tumor cells, that migrate towards TME and are transformed into cancer-associated fibroblasts (CAFs).

Distinguishing features of activated CAFs and quiescent fibroblasts are enhanced proliferation properties and ECM productivity (Procopio et al., 2015)(Alexander & Cukierman, 2016). CAFs do not only require self-metabolic reprogramming of glycolysis (Roy & Bera, 2016), but also reprogram the metabolism of TME (Kalluri, 2016). With the accumulated growth factors, cytokines, and stiffness, CAFs promote the progression of tumor in return, which formed a positive loop between cancer cells and CAFs. Activated CAFs induce tumour proliferation and metastasis through the secretion of growth factors, such as IL-6, insulin-like IGF, HGF, FGF-2, and PDGF, and modify TME by producing proangiogenic factors (Lin et al., 2011; Martino & Hubbell, 2010a; Pakravan et al., 2017). Moreover, tumor cells interact with CAFs by secreting growth factors and chemokines directly and through indirectly stimulating macrophages to influence fibroblasts. As a response, CAFs produce factors such as FGF-2, PDGF, and C-X-C motif chemokine 12 (CXCL12), which facilitate the proliferation of lung cancer cells (Figure 2) (Kuzet & Gaggioli, 2016; Terra et al., 2018).
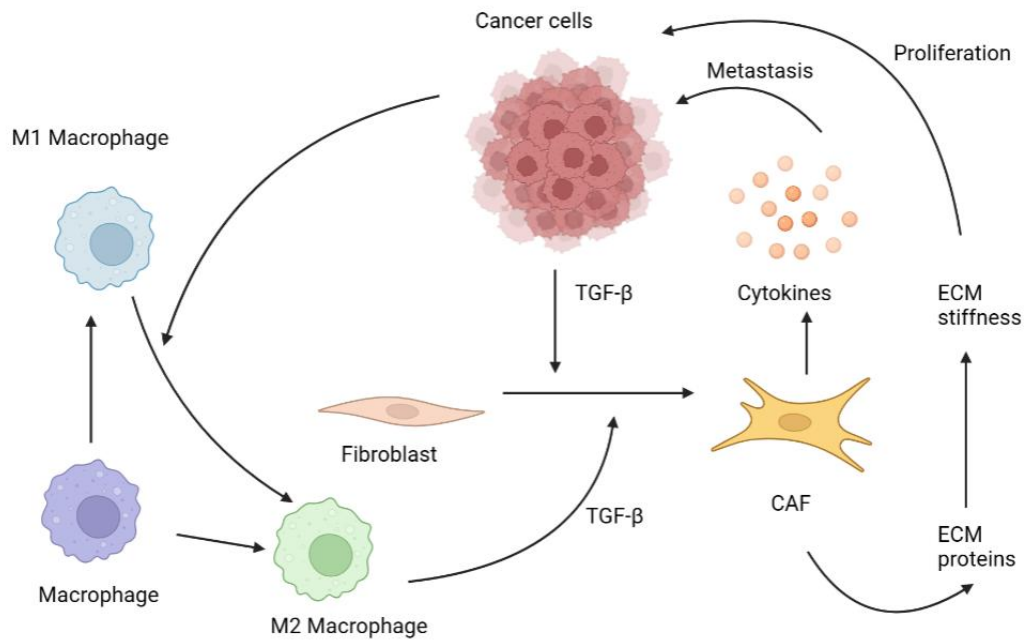
Figure 2. The interaction between CAFs and other cells in TME.

CAFs are activated by cancer cells and M2 macrophages. In return, CAFs regulate the cancer cells directly and M1 macrophages indirectly in TME. This figure was created with BioRender.com and modified according to the publication (Huang et al., 2021).

1.3.2. TAMs

Macrophages play an important role of immune reaction in the tumor microenvironment, which are activated to M1 and M2 subtypes due to the stimulation of different cells from the tumor microenvironment. Regarding their characteristics, M1s are related to bactericidal immune activity and the M2s are related to tumor remodeling processes. The tumor associated macrophages (TAMs) display the pro-tumorigenic features, such as progression, matrix remodeling and limitation of adaptive immunity, which are similar to the M2 subtype (Quatromoni & Eruslanov, 2012; ter Horst et al., 2015). In the clinic, high density of TAMs are associated with low overall survival rate in the lung cancer (LIN et al., 2015) and breast cancer patients

9

(Zhao et al., 2017). NSCLC patients with high density of M2 cells and highly expressed miR-130a are correlated with poor prognosis and increased tumor stage and metastasis (Hsu et al., 2018).

1.3.3. Fibronectin

Fibronectin (FN) is a basic component of the extracellular matrix (ECM) and it forms a polymeric fibrillar network to support cells (Figure 3). FN plays divers roles in cellular development, adhesion, migration, and wound healing, especially in tumors that up-regulate protein and receptor expression of ECM (Patten & Wang, 2021; VanSlykeBoswell & Musil, 2018). FN accumulated ECM also contains numerous growth factors and cytokines, including vascular endothelial growth factor, fibroblast growth factors, tumor necrosis factor, and more (Martino & Hubbell, 2010b; SackTeran & Nugent, 2016). Tumor cells with unsuccessful adhesion via integrin β1 limit the activation of proliferation signaling pathway and the tumor changes to the dormant state (Recasens & Munoz, 2019). The FN binding integrin stored in the ECM could awake the dormant cells to a proliferative state in the lung (Barkan et al., 2008; Di Modugno et al., 2018).
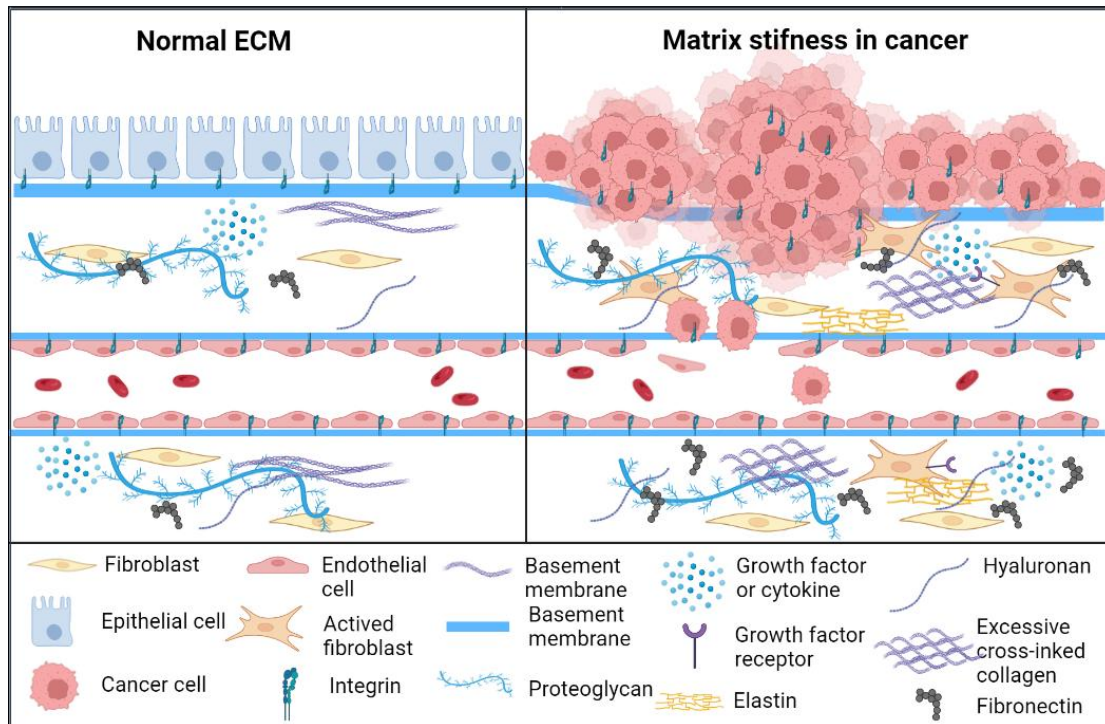
Figure 3. Extracellular matrix components in normal tissue (Left) and in tumor (Right). Fibronectin, collagen, elastin and hyaluronan are the main deregulation parts of ECM. This figure was created with BioRender.com and modified according to the publication (Huang et al., 2021).

1.4. Tissue Engineering Techniques in Lung Diseases

Tissue engineering is based on the development of biomaterials with the goal of assembling functional tissues and organs. Biological or artificial scaffolds, cells, growth factors and cytokines are commonly combined to reconstruct *in vitro* models to replace damaged tissue or test new drugs. For example, Chan and other colleagues generated a cutaneous coverage, which was seeded with isolated autologous stem cells from adipose tissue on a collagen consisting hydrogel. These cells were induced to differentiate into an epithelial layer, a vascularized dermal layer, and a hypodermal layer (Chan et al., 2012). In the field of lung disease, tissue engineering promoted the therapy both in clinical application and lung functional research (Kanzaki et al., 2013; Tan et al., 2017). In lung regeneration research, rat alveolar type II epithelial cells

were cultured in a 3D porous collagen scaffold forming a biomimetic collagen scaffold, which was implanted into the operative region of a rat partial lung resection model. Vascularization of this scaffold took place within 30 days, and this 3D biomimetic scaffold improved the general morphology recovery and functional alveolar-like structure formation of the injured lung (Wang et al., 2020). In the ECM of regenerated lung model, numerous molecules produced by different cells interact with each other, which provided a platform for the research on signaling pathways (GhaediNiklason & Williams, 2015; Hosseinirad et al., 2018).

1.5. Small Intestinal Submucosa Scaffold

Small intestinal submucosa (SIS) scaffold is a well studied decellularized material in the field of tissue engineering and regenerative medicine. SIS has a three-layer structure including *stratum compactum*, *muscularis mucosa,* and *submucosa* (Casarin et al., 2022; Kropp, 1998). In a modified approach, the mesentery with the vascular tree is removed and the mucosa layer is maintained to generate the SISmuc scaffold (Nietzer et al., 2016a). Porcine intestine is commonly used for SIS preparation (Figure 4), which firstly pass the decellularization step with detergents, chemicals and enzymes. Then the ECM sheet could work as graft directly or work as ECM hydrogel with solubilization treatment.

The first application of this material was reported in 1966 and the inverted small intestine was used as an autograft to replace the inferior vena cava in dogs (Matsumoto, Holmes, Burdick, Heisterkamp, & O'Connell, 1966). After decades of development, this material could not be only derived from porcine (Syed, Walters, Day, Kim, & Knowles, 2014), ovine (Rashtbar et al., 2018), bovine (ParmaksizElçin & Elçin, 2018), and rat (Totonelli et al., 2012), but also treated with lyophilization and pulverization process to prolong the self life and durability of SIS products (Cui et al., 2022).
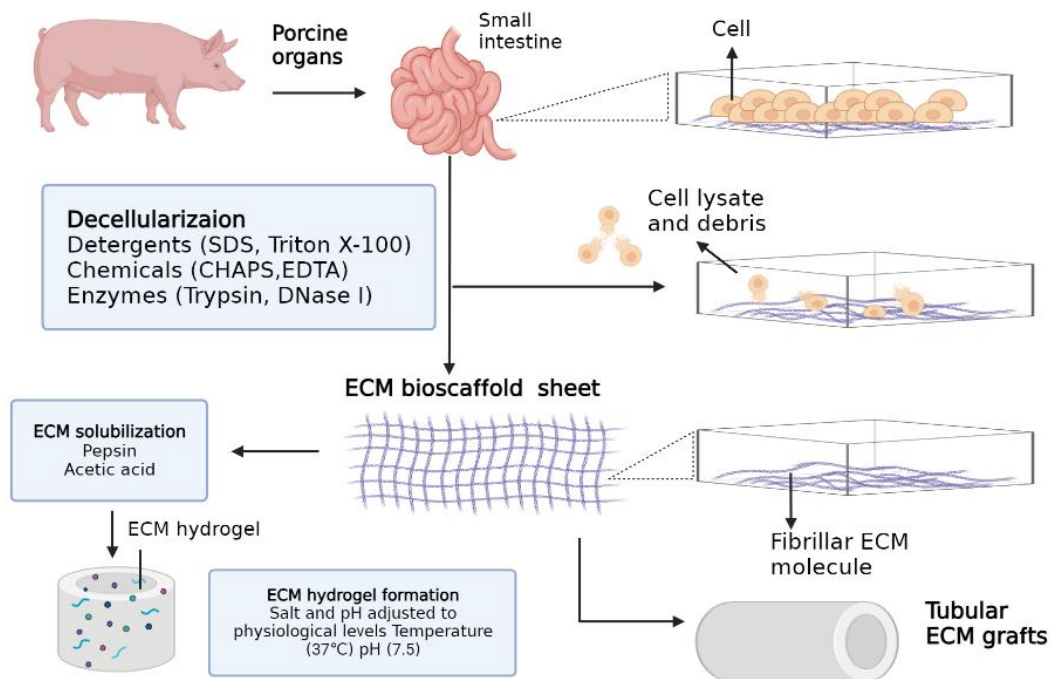
Figure 4. Process of preparing small intestinal submucosa (SIS).

The porcine SIS are derived from small intestine organs and they are made into three different products, ECM bioscaffold sheet, ECM hydrogel and ECM tubular grafts. This figure was created with BioRender.com and modified according to the publication (HusseyKeane & Badylak, 2017).

The suitable microenvironment of matrix encouraged scientists to culture different types of cells on SIS products. In the early stage, human microvascular endothelial cells and fibroblasts were cultured in hydrated SIS (Badylak, Liang, Record, Tullius, & Hodde, 1999). Further, both somatic cells and stem cells, patient-derived cells and cell lines were seeded on this material with different cultivation methods. In general, SIS could retain the original properties of cells and proliferation. Muscle-derived cells could remodel the SIS fast within the first ten days compared to the next ten days cultivation (Lu et al., 2005). Bone marrow derived-mesenchymal stem cells (Zhang, Lin, Frimberger, Epstein, & Kropp, 2005) and embryonic stem cells (Lakshmanan, Frimberger, Gearhart, & Gearhart, 2005) could grow and

differentiate in the SIS-ECM. The SIS sponge seeded with a mixture of dissociated epithelial and dermal cells could well differentiate and generate hair on mouse skin (Dong et al., 2019).

1.6. Aims

Lung cancer remains a significant global health burden, promoting the development of advanced experimental models for its study. *In vitro* 3D models provide a valuable platform to investigate the complex biology and tumor microenvironment of lung cancer, enabling the evaluation of various cultivation conditions and observation methods. This study aims to establish a robust *in vitro* 3D model using lung cancer tissue, including determining the optimal cultivation time, medium, and matrix for its growth, characterizing the model to identify key features of the tumor microenvironment, and improving observation methods for enhanced experimental outcomes.

The *in vitro* 3D model using lung cancer tissue is expected to enable the recreation of original tumor, compared to 2D model, with more physiologically relevant environment, expressing the cellular heterogeneity and spatial architecture. In this study the optimal cultivation time, medium composition, and type of matrix is determined to ensure 3D model viability and functionality. The 3D lung cancer model is characterized to determine its correspondence to the native tumor and to identify the tumor microenvironment. Histological staining, immunofluorescence staining, and DAPI staining will enable the assessment of cellular morphology, tumor markers, and cell proliferation associated with lung cancer. Furthermore, optimization of the cultivation conditions and observation methods will enhance the reproducibility and reliability of the lung cancer 3D model. Compared to the static culture, dynamic culture provides constant flow of culture medium for 3D model, which could carry out the metabolic products on time. This led to the hypothesis, that the dynamic culture could promote the cell proliferation of 3D lung cancer model.

With the refined model, better representation of the tumor microenvironment and improved experimental outcomes, we explore the new observation methods, which will enable accurate monitoring and analysis of tumor metabolism.

In summary, this study contributes to the growing knowledge on lung cancer and to the development of improved experimental models.

2. Materials

2.1. Biological Materials

2.1.1. Patient-Derived Tumor Samples

Tissue specimen from the tumor tissue were obtained from patients undergoing elective pulmonary resection for NSCLC at the Clinic of Cardiac and Thoracic Surgery at the University Hospital Magdeburg. Tumors were sampled after surgical resection by a pathologist to guarantee clear resection margins. Patients informed consent was obtained before surgery. The study was approved by the ethics committee of the medical faculty of the Otto-von-Guericke-University Magdeburg (vote 163/17, 16th October 2017).

2.1.2. Cells

We used primary human bronchial fibroblasts (hbFb) and the mouse swiss NIH embryo fibroblasts cell line (NIH-3T3) for co-cultivation. The hbFb were kindly provided by Julian Maurer (Experimental Thoracic Surgery Research Group, University Hospital Magdeburg), and the NIH-3T3 cell line by Prof Dr Andrea Kröger (Helmholtz-Center, Braunschweig).

Table 1. List of cells.

Cells	Description	Source
Human bronchial fibroblasts (hbFb)	Cells isolated from the bronchial tissue of patients from the clinic operation.	Julian Maurer (Hospital of Magdeburg University, Germany)
Mouse swiss NIH embryo fibroblasts cell line (NIH-3T3)	A cell line derived from mouse NIH/Swiss embryo cultures. It provided a convenient cell system for the study of murine sarcoma virus and DNA	Prof. Dr. Andrea Kröger (Helmholtz-Center, Braunschweig, Germany)

Cells	Description	Source
	transfection (JainchillAaronson & Todaro, 1969).	

2.1.3. SIS and SISmuc

The biological collagen scaffold was generated from decellularized porcine jejunum and provided by the Fraunhofer Institute for Silicate Research ISC Würzburg as described before (Hoppensack et al.; Jannasch et al., 2015; Schweinlin et al., 2017). During preparation of SIS, the two external layers of *tunica muscularis* and *tunica serosa* of the proximal jejunum were gently removed. Turning over the remaining intestine segment and the internal *tunica mucosa* is removed. In preparation of SISmuc, the mucosa layer is retained and only the mesentery with the vascular tree is removed before decellularization.

2.2. Solutions for Cell Culture

Table 2. List of solutions for cell culture.

Product	Specification	Producer/Supplier	Catalog number
DMEM high glucose	Cell culture medium	Gibco	31966-021
FBS superior stabil®	Fetal bovine serum	Bio & Sell	FBS.S.0615
PBS	Phosphate buffered saline (10x) without calcium and magnesium	Gibco	70011-036
Penicillin+ streptomycin+amphoteri	Antibiotics/antimycotics (100x)	Sigma-Aldrich	A5955

Product	Specification	Producer/Supplier	Catalog number
cin			

2.3. Enzymes and Inhibitors

Table 3. List of enzymes and inhibitors.

Product	Specification	Producer/Supplier	Catalog number
Accutase ®	cell detachment solution	Biozol	BLD-423201
Collagenase A	2.5 mg/mL	Merck	11088793001
Collagenase type IV	1 mg/mL	Merck	C4-22-1G
0.05% trypsin	Passage NIH-3T3 cells	Thermo Fisher	25300062

2.4. Antibodies

Table 4. List of primary antibodies.

Antigen	Clonality/species	Isotype	Dilution	Company	Order number
Alpha-smooth muscle Actin (1A4)	Mouse	IgG2a kappa	1:100	Invitrogen	14-9760-82
Fibronectin (FBN11)	Mouse	IgG1	1:100	Invitrogen	MA5-11981
MCT4 (Monocarboxylat transporter 4, SLC16A3)	Rabbit	IgG	1:100	Novus Biological	NBP1-81251

Antigen	Clonality/species	Isotype	Dilution	Company	Order number
p40 (BC28 Klon)	Mouse	IgG1	1:50	Zytomed Systems	ACI 3066A
P63 (GT1179)	Mouse	IgG1	1:100	GeneTex	GTX633818
TTF-1 (Thyroid transcription factor-1)	Mouse	IgG1 kappa	1:50	Zytomed Systems	MSK004-05

Table 5. List of secondary antibodies.

Antibody	Dilution	Company	Order number
Cy3-conjugated donkey anti-mouse IgG	IF: 1:500	Jackson ImmunoResearch	115-167-003
Cy3-conjugated goat anti-rabbit IgG (H+L)	IF: 1:500	Jackson ImmunoResearch	111-165-045
Cy3-conjugated goat anti-mouse IgG2a	IF: 1:500	Jackson ImmunoResearch	115-167-186

2.5. Chemicals

Table 6. List of chemicals.

Product	Specification	Producer/Supplier	Catalog number
DAPI	4',6-diamidine-2-phenylindole dihydrochloride	Sigma-Aldrich	D9542-10mg
DMSO	Dimethyl sulfoxide	C. Roth	A994.2
Ethanol	96% ethanol, denaturation	Th. Geyer	2206
Mitomycin C	Cytostatic agent	Sigma-Aldrich	M0503-2mg
Normal	Donkey serum	Bio-Rad	C06SB

Product	Specification	Producer/Supplier	Catalog number
donkey serum (NDS)			
Normal goat serum (NGS)	Goat serum	Sigma-Aldrich	S26-100ML
PFA	Paraformaldehyde	C. Roth	0335.1
Roti ® Histokitt	Embedding medium	C. Roth	6638.1
Tx100	Triton ™ X-100	Sigma-Aldrich	X100-500ML
Roti®-mount	Embedding medium with xylol 100mL	C. Roth	HP68,1
Xylol	2.5L	Dr.K.Hollborn&Söhne	215-535-7
ProClin	50mL	Sigma	49376-U
Glycerin	500mL	Sigma	G5516
Aqua B. Braun	1000mL	B. Braun	0082479E
NaCl	Sodium chloride	C. Roth	9265.2
KCl	Potassium chloride	C. Roth	6781.3
Na2HPO4 x 2H2O	Disodium hydrogen phosphate dihydrate	C. Roth	4984.1
Isopropanol	2-Propanol	C. Roth	9866.1
KH 2PO 4	Potassium dihydrogen phosphate	C. Roth	3904.2

2.6. Prepared Solutions

Table 7. List of prepared solutions.

Solution	Composition
10x PBS $^-$(1 litre)	80 g NaCl, 2 g KCl, 14.4 g Na2HPO4 x 2H2O, 2.4 g KH2PO4 in 1L sterile water.
DAPI in PBS $^-$(50mL)	1:10000, 5 microliters DAPI in 50 mL PBS $^-$
Mowiol 4-88 DABCO	6.0 g glycerin +2.4 g Mowiol 4-88 +6.0 mL Aqua dest. +12.0 mL 0.2 M Tris-HCl +25 mg/mL DABCO
NDS in PBS $^-$ + Proclin + Tx-100 (50mL)	1.5 mL normal donkey serum (= 3%) +48.5 mL PBS $^-$ + 5 µl Proclin (= 0.01%) + 5 µl Tx100 (= 0.01%)
NGS in PBS $^-$ + Proclin + Tx-100 (50mL)	1.5 mL normal goat serum (= 3%) +48.5 mL PBS $^-$+ 5 µl Proclin (= 0.01%) + 5 µl Tx100 (= 0.01%)
Trypan blue solution (50mL)	0.4% Trypan Blue Solution 5 mL +45 mL PBS $^-$
Hemalaun solution acid acc. to Mayer	C. Roth T865.1. Ready to use.
Eosin Y solution	C. Roth X883.1. Ready to use.

2.7. Kit

Table 8. List of Kit.

Name	Specification	Manufacturer	Commodity number
M30 ELISA Kit	M30 CytoDeath™ ELISA	TECOmedical GmbH	10900

2.8. Laboratory Equipment

Table 9. List of laboratory equipment.

Laboratory equipment	Manufacturer
Autoclave: Laboklav 55-195	SHP Steriltechnik AG
Centrifuge: Allegra X-12R centrifuge	Beckman Coulter
Centrifuge: Sprout® plus	Fisherbrand
CO2 incubator: MCO-19AICUV-PE	Panasonic
Cryostat: CM 1950	Leica
Microplate reader: Infinite ® M Plex	TECAN
Dynamic 3D culture incubator with peristaltic pump	Fraunhofer ISC Würzburg
Freezer: -20 ° C -30 ° C (Biomedical Refrigerator MDF-U5312) -80 ° C (KM-DU73Y1 ultra-low temperature refrigerator) -150 ° C (MDF-C2156VAN-PE ultra-low temperature refrigerator)	 Liebherr Panasonic Panasonic Panasonic
Hot air sterilizer: Heraeus Oven	Thermo Fisher Scientific
Ice maker: 105587	ZIEGRA ice machine co., ltd
Lab dish washer: G7835 CD	Miele Professional
Microscope: Evos Auto FL 2 AMAFD2000	Thermo Fisher Science Corp.
Microscope: Evos XL Core AMEX 1000	Thermo Fisher Science Corp.
Multi-channel pipette VB-0964, 10-100 µ l	Eppendorf
Pipettes: 0.1-2.5 microliters 0.5-10 microliters 2.0-20 microliters	 All from Eppendorf

Laboratory equipment	Manufacturer
10-100 microliters 20-200 microliters 100-1000 microliters	
Pipetus 9907200	Hirschmann
Safety cabinet: Herasafe KS	Thermo Fisher Scientific
Shake water bath: 1083	GFL
Shaker: KS 501 Digital	Ika
Suction system: VACUBOY 155 500	Integra
Ultrapure water treatment system: Millipore Milli-Q ™ Z 00 QSVC01	Merck
Vacuum pump: ME 4C NT	Vacuubrand
Vortexer: Lab Dancer S040	VWR
Fume hood	Wesemann Laboreinrichtungen
Magnetic stirrer	IKA
pH meter	Mettler Toledo

2.9. Laboratory Materials

Table 10. List of laboratory materials.

Name	Specification	Manufacturer	Order number
Beaker	600 mL 1000 mL	Simax	DI60743538121711 DI60743528122051
Cell crowns for three-dimensional culture	Inner diameter: Outer 12: 17mm Material: Metal	Fraunhofer Institute for Silicate Research ISC, Würzburg, Germany	

Name	Specification	Manufacturer	Order number
Manual counter	For cell counting	Infactory	4022107175012
Staining through	For 10 slides	Assistent	41205
Tweezers	Universal tweezer ESD	Knipex	92 38 75 ESD

2.10. Consumables

Table 11. List of consumables.

Name	Specification	Manufacturer	Order number
Adhesion microscope slides	25 × 75 ×1 mm	Epredia	J1800AMNZ
Minisart	Filter unit 0.2µm	Sartorius	211690103
Cell culture flask	T75 (75) cm^2 T25 (25) cm^2	VWR VWR	TPPA90076 TPPA90026
Cover slips	24 × 50 mm #1	Epredia	BB024050A1
Eppendorf Tips	0.1-10 ul 2-200ul 50-1000ul	Eppendorf	0030000811 0030000870 0030000919
Filter paper	Type 600P	C. Roth	CA20.1
Gloves	M/7-8 L/8-9	B.BRAUN	9208429 9208437
Laboratory and hygienic wipe	150 double-ply	Zellstoffvertriebs GmbH & Co. KG (ZVG)	16515
Model 819 narrow band unidirectional blade	Cryostat blade	Leica	14035838382

Name	Specification	Manufacturer	Order number
O-rings (sealing rings) for bioreactors	MVP 70 rot	VWR	21444
Parafilm	for covering or sealing vessels	Bemis	PM-999
Pasteur pipettes, without cotton stopper	150mm	C. Roth	4518
Pump tubes PharMed® BPT	ID: 2,79 mm L＝ 381mm+ 2 Manchons	Saint-Gobain performance plastics	ISMCSC0746 (VWR)
Safe seal microcentrifuge tube	0.5 mL 1.5 mL 2.0 mL	Eppendorf	0030121023 0030120086 0030120094
Sample bags	W 100 × H 150 mm	C. Roth	P279.2
Scalpel	Disposable	C. Roth	T997.1
Serological pipet	5mL 10mL 50mL	Corning	4487 4488 4490
Tygon® 3350 Silicone tube	ID 3.2mm, OD 6.4mm, Wall 1.6mm	Saint-Gobain performance plastics	4330423 (Kleinfeld-Labor Shop)
TC Dish 150	Standard	SARSTEDT AG & Co. KG	83.3903
Tissue culture dish 60	22.1 cm^2	TPP	93060
Tissue-Tek	tissue embedding for cryo-section	Sakura Finetek	4583

Name	Specification	Manufacturer	Order number
Tissue-Tek freezing mold	25x20x5 mm	Sakura Finetek	4557
Centrifuge tubes	15mL 50mL	Greiner Bio-one	188271-N 227261
Well plate of cell culture	12 well	Nunc	734-2156
Freezer Container	Mr. Frosty	Thermo Scientific	5100-0001
Cryo tubes	2mL	Greiner Bio-one	E22113MV
Counting chamber	Neubauer-improved	MARIENFELD	0640010

2.11. Software

Table 12. List of software.

Software	Description	Development/sales
ImageJ	Cell counting	Wayne Rasband
NoteExpress	Citation program	Swiss academic software
Prism 9	Statistical programme	GraphPad software
i-Tan control	Absorption measurement	Tekan
Microsoft Excel	Patients information form	Microsoft
Microsoft Power Point	Figures processing	Microsoft
Microsoft Word	Word processing	Microsoft
WPS office	Office processing	Kingsoft Office Software
Windows 10	Computer software	Microsoft
BioRender	Figures processing	Created with BioRender.com

3. Methods

3.1. Cell Culture Basics

For cell culture work, the incubator was set to standard conditions with 37°C, 5 % CO_2, and 95 % humidity. Cell culture media in static culture were exchanged every two to three days, while in dynamic culture the medium was exchanged once a week. All used products and liquids were purchased sterile, autoclaved or sterile-filtered. If possible, all used instruments were cleaned with disinfectant then autoclaved at 121°C for 90 min or sterilized in 180°C oven for three hours.

3.2. Cell Cultivation

Human primary bronchial fibroblasts (hbFb) were cultivated with DMEM medium containing 10% FCS. The mouse swiss NIH embryo fibroblasts cell line (NIH-3T3) was cultured in DMEM medium with 10% FCS and passaged with 0.05% trypsin and the digestion process was stopped with the same amount of cultivation medium. Isolated tumor cells were cultured with DMEM, 10% FCS, and 1% antibiotics-antimycotic solution.

3.3. Isolation of Tumor Cells for 2D Cell Culture

One part of the tumor biopsy was embedded with Tissue-Tek® O.C.T. Compound and stored at -80°C as positive control. The other half of the tumor tissue was minced into 1 - 1.5 mm3 pieces which were washed three times with PBS to remove blood and necrotic cells. Then the tumor pieces were digested using either 2.5 mg/mL collagenase A or 1 mg/mL collagenase type IV. The amount of enzyme solution corresponded to five times the volume of the tumor pieces. For digestion, the samples were shaken continuously in the water bath at 37°C. Every 30 minutes, the supernatant was collected and the

digestion was stopped with the same volume of serum-containing medium, while the solid residues were incubated with fresh enzyme solution. After all solid tissue was digested, cells were centrifuged at 200g for 3 min. Cell pellets were suspended in the medium. The cells were cultured for 21 days on 6 cm petri dishes under standard culture conditions.

3.4. Generation and Cultivation of Static 3D Lung Cancer Model

The scaffold of SIS or SISmuc were cut into 1.5 x 3 cm pieces (Figure 5A-G). The tumor pieces were seeded between two layers of the scaffold without air bubbles. The 3D model with "sandwich" structure was fixed between two customized cylinders (cell crowns), transferred to a 12-well plate, and cultured in DMEM medium with 10% FCS and 1% antibiotics-antimycotics solution. The cell cultures were checked for contamination with the microscope after overnight cultivation. The medium was exchanged every two to three days. The static 3D models were cultured for 21, 28, and 42 days under standard culture conditions. At the respective days, the 3D models were embedded with Tissue-Tek® O.C.T. Compound and stored at -80°C for further analysis.
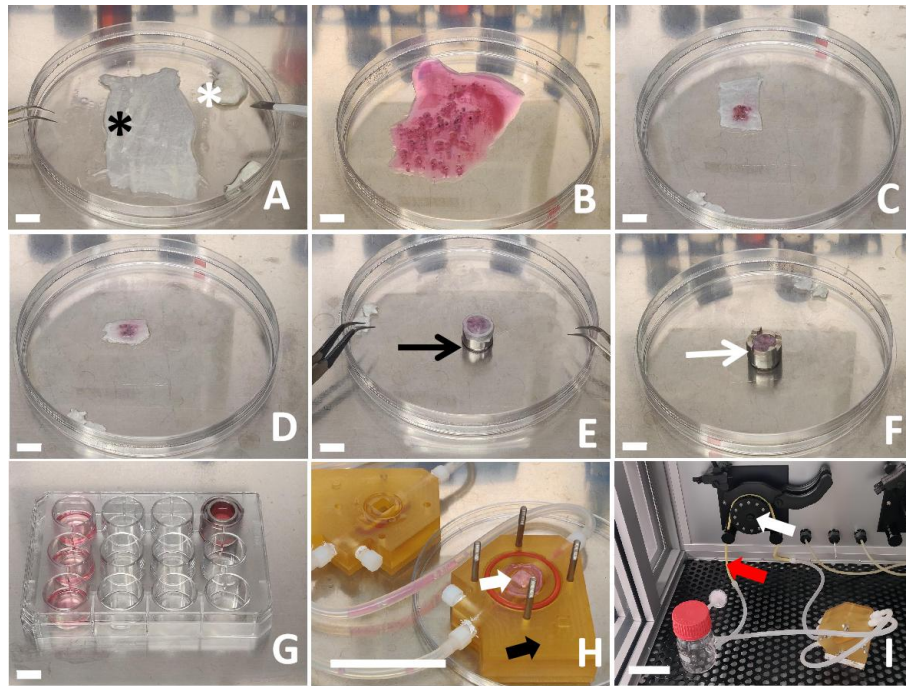
Figure 5. The generation and composition of three-dimensional (3D) models.

The static 3D model of lung cancer (A-G). (A) The small intestinal submucosa (SIS) biological matrix (black asterisk) is trimmed to fit the customized receptacle (cell crown). Residues are removed (white asterisk). (B) Tumor tissue form surgical specimen is cut into 1-1.5mm3 pieces. (C,D) Tumor pieces are embedded between two layers of trimmed SIS. (E,F) The "sandwich culture" is stretched on the inner metal crown (black arrow) and fixed with the outer metal crown (white arrow). (G) The "sandwich" model is covered with culture medium and cultured in a 12 well plate. (H) For dynamic tissue culture conditions the "sandwich" model (white arrow) was transferred onto the bioreactor platform (black arrow). (I) A pulsatile medium flow is established using a closed perfusion circuit (red arrow) and a peristaltic roller pump (white arrow). Scale bar represents in A-G as 1 cm and in H and I as 6 cm.

3.5. Generation and Cultivation of Dynamic 3D Lung Cancer Model

After the 3D models were cultured overnight and contamination was ruled out, they were transferred into the bioreactor chamber for dynamic culture (Figure

5H-I). The customized bioreactors described before (Nietzer et al., 2016b) were perfused with tissue culture medium (50 mL DMEM with 10% FCS and 1% antibiotics-antimycotics solution) using a peristaltic pump at a speed of 3 rpm providing a medium flow of 1.5 mL/min. The medium was exchanged every seven days. The 3D models were cultured for 21 and 28 days, respectively, under standard culture conditions. At the end of the experiment, they were embedded with Tissue-Tek® O.C.T. Compound and stored at -80°C for further analysis.

3.6. Co-Cultivation with Either Human Bronchial Fibroblasts or NIH-3T3 Cell Line

The NIH-3T3 cells were mitotically inactivated using 4 µg/mL Mitomycin C for 2h kept under standard culture conditions and afterwards washed five times with PBS. For co-cultivation, hbFbs or NIH-3T3 cells were seeded with 0.15 million cells per well in the 12 well plate and cultivated under standard conditions. When the cell confluency reached 80%, the cell crowns of the static 3D models were transferred into the corresponding wells and cultured with DMEM medium with 10% FCS and 1% antibiotics-antimycotics solution. The wells containing hbFb were changed every week and the wells with mitotically inactivated NIH-3T3 were changed every two weeks.

3.7. Cutting of Cryo Samples

To prepare the frozen sections, the freezing mold was labeled on the middle line of the sample. After storage at -80 °C, the sample was first put at -20 ° C for 20 minutes. The frozen model was cut at the middle line and five 10 µm sections were put on one glass slide.

3.8. Histological and Immunofluorescence Staining

The haematoxylin–eosin staining was performed with the following protocol.

Table 13. Hematoxylin and Eosin staining protocol.

Step	Solution	Time
Staining the basophilic structures	Haematoxylin	25 Min
Rinsing	Tap water (warm and flowing)	30 Min
Checking the blue staining	Under microscope	Until blue
Staining the acidophilic structures	Eosin	4 Min
Rinsing	Deionized water	2 seconds
Dehydration	Ethanol 70%	2 seconds
	Ethanol 80%	2 seconds
	Ethanol 90% I	10 Min
	Ethanol 90% II	10 Min
	Air (room temperature)	10 Min
	Xylol I	10 Min
	Xylol II	10 Min
Mounting	Roti®-Histokitt	Overnight

For immunofluorescence staining, samples were fixated using a 4% paraformaldehyde solution for 10 minutes at room temperature (RT). The samples were blocked dependent on the used secondary antibody with either normal goat or normal donkey serum in PBS for 30 minutes at RT. Primary antibodies were diluted in blocking serum and incubated overnight at 4°C in a humidified chamber. The unbound primary antibodies were washed away with PBS for three times. The secondary antibodies were diluted in blocking serum

and incubated for 1 hour at RT. Finally, the unbound secondary antibody was removed with PBS and the sections were incubated with 1µg/mL DAPI in PBS for 10 minutes at RT. The sections were washed three times in PBS and embedded in Mowiol 4-88 with DABCO (2.5%). As for negative control, the primary antibody was omitted.

3.9. Imaging Process

HE staining images and cell culture images were taken using EVOS™ XL Core Imaging System. Immunofluorescence staining images were taken using Invitrogen EVOS FL Auto 2.0 Imaging system. A tiled photo was the combination of ten-fold photos which covered the whole area of the sample under the microscope. According to the shape of the sample, several central points of ten-fold photos were selected by hand and then merged to get one tiled photo.

3.10. Success Rate Evaluation

Based on the classification of lung cancer (Travis et al., 2013; Yatabe et al., 2019), we created the criteria for our models. In 2D culture, successful cell cultivation was determined by morphological appearance using light microscopy according to the following criteria: I) two or more different cell types were identified according to cell morphology, II) lung cancer cell colonies possessed specific cancer morphological features (irregular cell size and shape; enlarged nuclei; increased nuclei-cytoplasm ratio; abnormal cellular structures, such as cytoplasmic vacuoles, multi-nuclei; intercellular bridges). In 3D culture, criteria were evaluated following HE and IF staining: I) two or more different types were identified, II) two or more tumor-specific structures (cancer colony; tissue necrosis; cell invasion into normal tissue, and III) expression of lung cancer specific markers (TTF-1, p40/ p63) according to the pathology report of patients.

3.11. M30 Detection of Epithelial Cell Apoptosis

The M30 CytoDeathTM ELISA was used to detect the epithelial cell apoptosis by quantitative determination of the soluble caspase-cleaved keratin 18 (cck18) Asp396 (M30) neo-epitope. The release of the antigen into the cultivation medium occurs due to secondary necrosis of apoptotic bodies. The sample media were collected every 7 days from each 3D model. The ELISA was performed according to the manufacturer's protocol. The samples were measured in duplicates. Samples with too high concentration were diluted to half with the corresponding cell culture medium to fit the range of the standard curve from 0-3000 U/L. After incubation on an orbital shaker (600 rpm) for 4 hours, wells were washed five times prior to the addition of the substrate. The reaction was stopped after 20 minutes. Absorbance was measured with a microplate reader after 10 sec shaking and five minutes of waiting. According to the standard curve fitted with cubic spline algorithm, the concentration of cck18 was calculated for every sample.

3.12. The Thickness and Cell Density Evaluation of 3D Models

The thickness of 3D tissue models was measured using the software Image J. Five tiled ten-fold images were selected from non-overlapping regions of each sample. In the images, 3D models should contain cells stained with DAPI, original tumor pieces and biological matrix with autofluorescence. With the threshold, selection area and segmented line tool in Image J, the area and the centerline of each 3D model were measured. The thickness was calculated by the following formula:

$$\text{Thickness (μm)} = \frac{\text{Area of 3D model (μm}^2\text{)}}{\text{Centerline(μm)}} \qquad (1)$$

Cells in the 3D model were counted automatically and by manual counting using the same software Image J . Five non-overlapping images (ten-fold magnification) and five overview images (tiled with ten-fold magnification) of DAPI staining per model were used to determine the cell number through Image J Macro. The Image J Macro used for counting DAPI-positive cells number:

run("8-bit");

//run("Brightness/Contrast...");

run("Enhance Contrast", "saturated=0.35");

setAutoThreshold("Default");

//run("Threshold...");

setAutoThreshold("Default dark");

//setThreshold(25, 255);

setOption("BlackBackground", false);

run("Convert to Mask");

run("Watershed");

run("Analyze Particles...", "size=10-Infinity show=Outlines display summarize in_situ");

The merged DAPI staining and autofluorescence images were used to measure the area of the 3D model. In the ten-fold magnification image, two layers of matrix, tumor pieces, and cells should be included. The ten-fold magnification images represent the tumor area of the 3D model, while the tiled images represent the whole section of the 3D model. The cell density was calculated by the following formula:

$$\text{Cell density (cells/mm}^2) = \frac{\text{Cell number (cells)}}{\text{Area of 3D model (mm}^2)} \qquad (2)$$

3.13. Statistical Analysis

Statistical significance of the success rate and the lung cancer colony rate was determined using the Fisher's exact test. The unpaired t-tests or the one-way

ANOVA and Tukey-test were used for analyzing the thickness and the cell density in static 3D model and the cell density comparison of the static 3D model and the dynamic 3D model. Mann-Whitney U test was used to analyze the thickness differences between static and dynamic 3D models. Kruskal-Wallis test was used for comparing multiple groups (M30 ELISA). The p-values ≤ 0.05 were considered significant; *: $p \leq 0.05$; **: $p \leq 0.01$; ***: $p \leq 0.001$. Diagrams were designed with Prism 9.

4. Results

4.1. General Information about the Patients

In this study, tumor samples from 21 patients (age range 48-83 years) were analyzed in 2D and 3D culture (Table 14): One case was a small cell lung cancer (SCLC), 20 cases were non-small cell lung cancer (NSCLC) with 14 cases of adenocarcinoma (ADC) and 6 cases of squamous cell carcinoma (SQCC) (Table 15).

Table 14. Patients characteristics

Nr.	Patient number	gender	age (y)	BMI	FEV1 (%)	smoking history	pack years
1	#75	Male	61Y	18	77	smoker	30
2	#76	Male	63Y	28	67	former smoker	55
3	#78	Male	78Y	34	56	former smoker	30 - 40
4	#79	Male	63Y	32	77	former smoker	30
5	#83	Female	54Y	17	71	smoker	35
6	#84	Male	68Y	24	42	former smoker	30
7	#87	Male	65Y	25	-	former smoker	30
8	#89	Male	72Y	24	49	smoker	6
9	#91	Female	76Y	25	96	smoker	40
10	#92	Male	67Y	31	92	former smoker	20
11	#94	Male	65Y	45	32	smoker	20
12	#96	Male	72Y	21	68	never smoker	
13	#107	Female	62Y	25	74	smoker	40
14	#109	Male	51Y	29	78	smoker	30
15	#110	Female	48Y	35	79	smoker	20 - 30
16	#111	Female	61Y	24	61	smoker	50
17	#125	Female	83Y	20	108	former smoker	10

Nr.	Patient number	gender	age (y)	BMI	FEV1 (%)	smoking history	pack years
18	#126	Female	78Y	20	-	never smoker	
19	#130	Female	80Y	25	102	never smoker	
20	#132	Female	65Y	19	90	never smoker	
21	#135	Male	49Y	19	77	smoker	25

Table 15. Tested tumour tissue

Nr.	histology	TTF-1/p63/p40 expression	TNM classification	tumor localization	induction therapy	type of surgery
1	pulmonary adenocarcinoma	Not mentioned	pT1b pN0(0/32) L0 V0 Pn0 R0 G3 cM0	left upper lobe	no	lobectomy
2	pulmonary squamous cell carcinoma	p40+	pT3 pN0(0/31) L1 V0 Pn0 R0 G3 cM0	right upper lobe	no	lobectomy
3	pulmonary adenocarcinoma	Not mentioned	pT1c L1 V0 Pn0 R0 G2 cMx	right lower lobe	no	lobectomy
4	pulmonary adenocarcinoma	TTF-1+	pT1c pN0(0/14) L0 V0 Pn0 R0 G2 cM0	right lower lobe	no	lobectomy
5	small cell lung cancer	Not mentioned	ypT0 pN0 (0/7) V0 R0	right upper lobe	yes	lobectomy
6	pulmonary squamous cell carcinoma	p40+	pT4 pN1(1/17) L1 V1 Pn1 R0	left upper and lower lobe	no	pneumonectomy
7	pulmonary squamous cell carcinom	Not mentioned	pT1c pN0 (0/18) L1 V0 Pn0 R0 G3 cM0	right lower lobe	no	segmentectomy
8	pulmonary squamous cell carcinom	Not mentioned	pT2a pN0 L0 V1 R0 G2 cM0	right upper lobe	no	lobectomy
9	pulmonary adenocarcinoma	TTF-1+	pT2b pN0 (0/16) L0 V1 Pn0 R0 G3	left upper lobe	no	lobectomy
10	pulmonary adenocarcinoma	TTF-1+	pT3 pN0 (0/4) L1 V1 Pn1 R0 G3 cM0	right lower lobe	no	bi-lobectomy

Nr.	histology	TTF-1/p63/p40 expression	TNM classification	tumor localization	induction therapy	type of surgery
11	pulmonary squamous cell carcinom	p40+	pT4 pN0 (0/9) G3 L0 V0 R1	right lower lobe	no	lobectomy +segmentectomy
12	pulmonary adenocarcinoma	TTF-1+	pT3 pN0 (0/17) L1 V1 Pn0 R0 G2 cM1b	left upper lobe	no	lobectomy
13	pulmonary adenocarcinoma	TTF-1+	pT2 pN1(1/10) L1 V1 Pn0 R0 G2	right upper lobe	no	lobectomy
14	pulmonary adenocarcinoma	TTF-1+	pT3 pN0 (0/35) G3 L0 V0 Pn0 R0 cM0	right upper lobe	no	lobectomy
15	pulmonary adenocarcinoma	TTF-1+	pT2a pN0 (0/22) L1 V0 Pn0 R0 G3 cM0	right upper lobe	no	lobectomy
16	pulmonary adenocarcinoma	TTF-1+	pT1c pN1 (1/5) L1 V0 Pn0 R0 G2 cM0	left upper lobe	no	lobectomy
17	pulmonary adenocarcinoma	Not mentioned	pT1c pN0(0/22) L0 V1 Pn0 R0 G2	left upper lobe	no	lobectomy
18	pulmonary adenocarcinoma	Not mentioned	pT2a pN2(4/18) L1 V1 Pn0 R0 G2	left upper lobe	no	tri-segmentectomy
19	pulmonary adenocarcinoma	TTF-1 weak positive	pT1b pN0(0/16) L1 V1 Pn0 R0 cM0	left lower lobe	no	lobectomy
20	pulmonary adenocarcinoma	Not mentioned	pT4 pN0(0/40) L1 V0 Pn0 R0	right upper lobe	no	pneumonectomy
21	pulmonary squamous cell carcinoma	Not mentioned	pT2b, pN2(9/38), L1, V0, Pn0, R0, G3,cM0	right lower lobe	no	lobectomy

Patients information. SQCC: squamous cell carcinoma; SCLC: small cell lung cancer;

ADC: adenocarcinoma. +: positive expression; -: negative expression; +/-: weak

positive

4.2. Success Rate and Lung Cancer Colony Rate in 2D and Static 3D Culture

At first, we compared the success rate and the lung cancer colony rate of 2D and static 3D cultivation. According to the cell morphology, cultures with tumor cells were obtained from three samples in 2D and 15 samples in 3D after 28 days of cultivation (Figure 6A). The success rate in 2D culture was 19% (3/16) with one ADC, two SQCC, and zero SCLC. In static 3D culture, the success rate was 94% (15/16) with nine ADC, five SQCC, and one SCLC. The higher success rate in 3D cultures was significantly different from 2D cultures ($p < 0.001$). Lung cancer colonies were detected in three cases of 2D cultures and in twelve cases of static 3D cultures (Figure 6B). The rate of lung cancer colony in the static 3D culture was with 75% (12/16) significantly higher than in 2D culture with 19% (3/16) ($p < 0.01$). These data suggest that static 3D culture effectively supported the *in vitro* cultivation of the tumor cells.
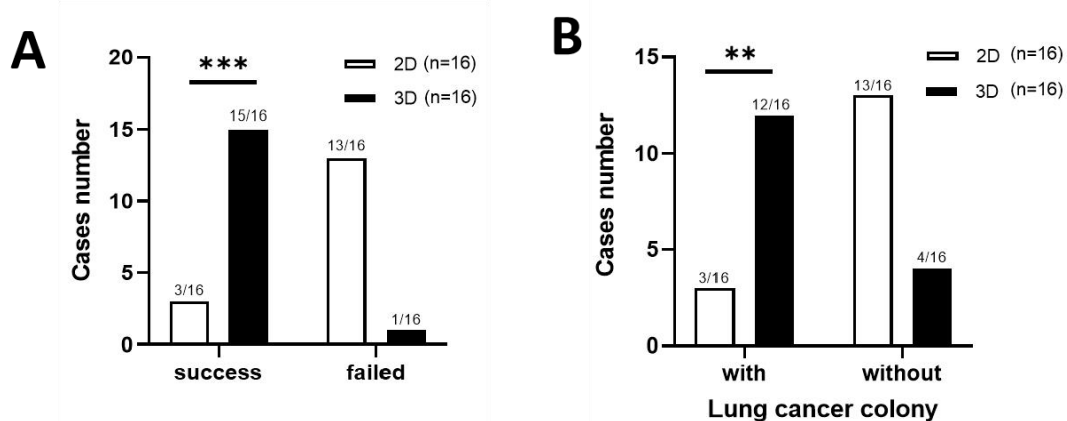

Figure 6. Comparison of 2D and static 3D models.

(A) Success rate and (B) lung cancer colony rate in 2D and static 3D models. Significance was determined using the Fisher's exact test. *: $p \leq 0.05$; **: $p \leq 0.01$; ***: $p \leq 0.001$.

4.3. Morphological Features of the 2D and the Static 3D Culture Model

In 2D culture, cells possessed a flat morphology and grew as monolayer. The cancer colonies were surrounded by fibroblast-like cells and possessed vacuoles in some of the cells (Figure 7A). The cancer colonies were easy to identify during the first three weeks of cultivation. They possessed clear intercellular bridges and higher nuclei-cytoplasm ratio compared to other cells (Figure 7B). The three-layer structure of the "sandwich" culture could be identified in the static 3D model (Figure 7C, D). In the view of the tiled photo, tumor pieces occupied the main space of the static 3D model. Tumor pieces were connected to the SIS matrix. The two layers of SIS matrix attached with each other when there was no tumor piece (Figure 7E). According to the cell distribution in the static 3D model, we defined three regions: (1) tumor area, (2) interface between tumor and matrix, and (3) the matrix which was infiltrated with cells. The static 3D models maintained the cancer colonies which were derived either from SQCLC (Figure 8), ADC, or SCLC (Figure 9). The diagnosis were made by pathology department with the original tumor while all 3D models had no diagnosis from the pathology department.
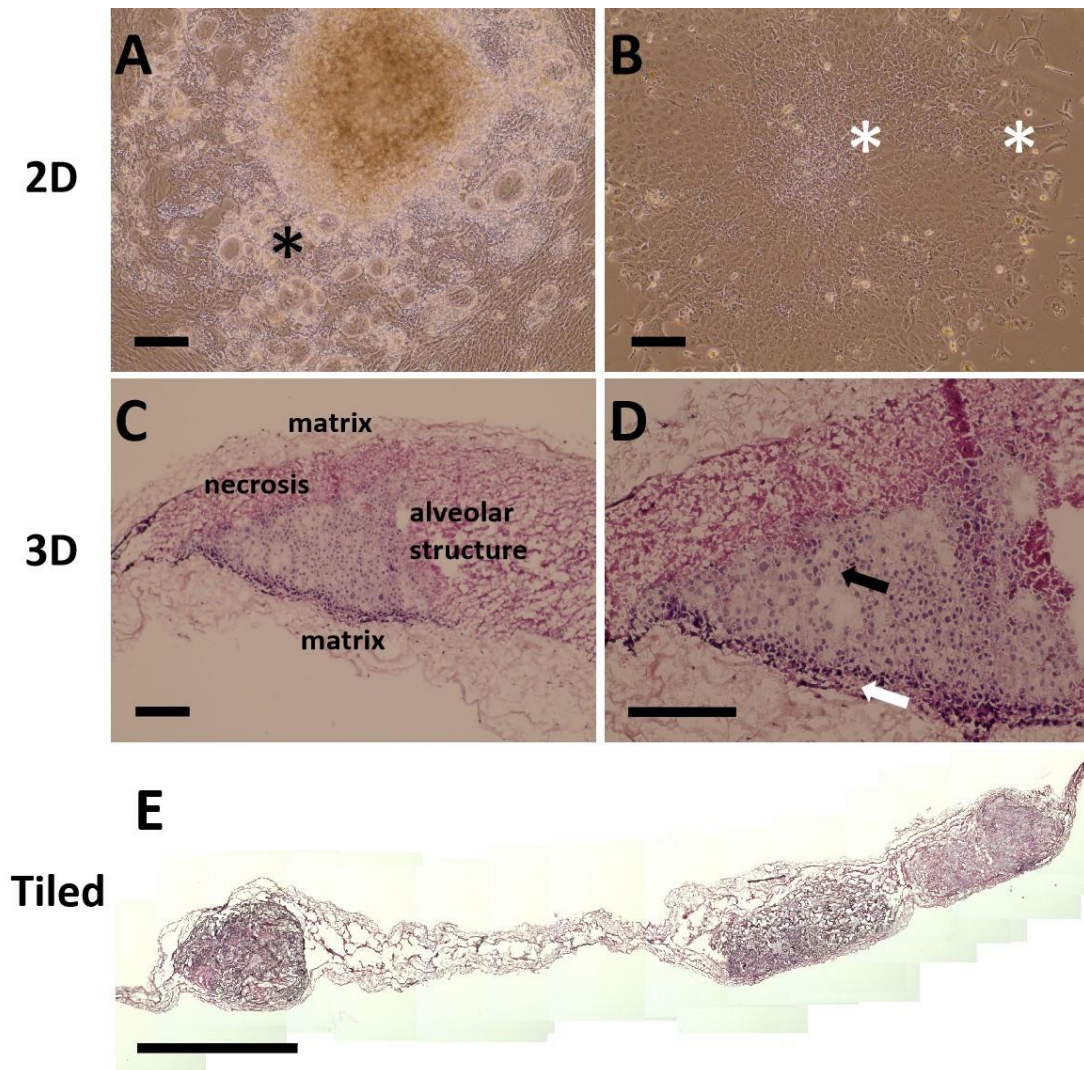
Figure 7. Morphological features of 2D and static 3D models.

(A) Lung cancer cells were identified by irregular cell size and shape, enlarged nuclei, and cytoplasmic vacuoles (black asterisk). (B) Increased nuclei-cytoplasm ratio, multi-nuclei, and intercellular bridges were identified in 2D culture (see white asterisks). (C) In hematoxylin-eosin (HE) stained sections of static 3D culture, there are two layers of matrix covering the original lung tumor pieces. Within the static 3D model, we could identify original alveolus structures and necrosis area. (D) Several types of cells existed in static 3D model with different morphology. Lung cancer cells are labelled with a black arrow and non-cancer cells with a white arrow. (E) Tiled HE photo of static 3D model. Sever tumor pieces are covered with SIS matrix on top and

41

bottom side, which formed "Sandwich" structure. Scale bar represents 200 µm in A-D, 1000 µm in E.

No.6 SQCC   No.8 SQCC   No.11 SQCC

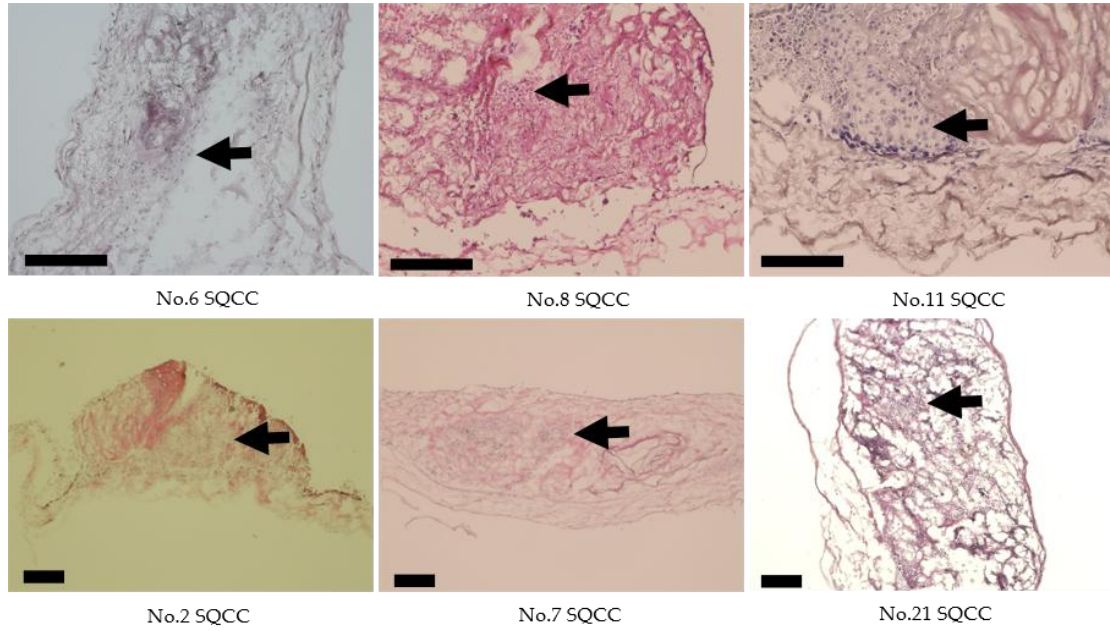No.2 SQCC   No.7 SQCC   No.21 SQCC

Figure 8. The morphology of squamous cell lung cancer 3D models.

HE stainings of static 3D sandwich models of patient number 6, 8, 11, 2, 7, and 21.

SQCC: squamous cell carcinoma; Black arrow: lung cancer cells. Scale bar = 200 µm.

No.1 ADC

No.3 ADC

No.4 ADC

No.9 ADC

No.10 ADC

No.12 ADC

No.13 ADC

No.14 ADC

No.15 ADC

No.16 ADC

No.17 ADC

No.18 ADC

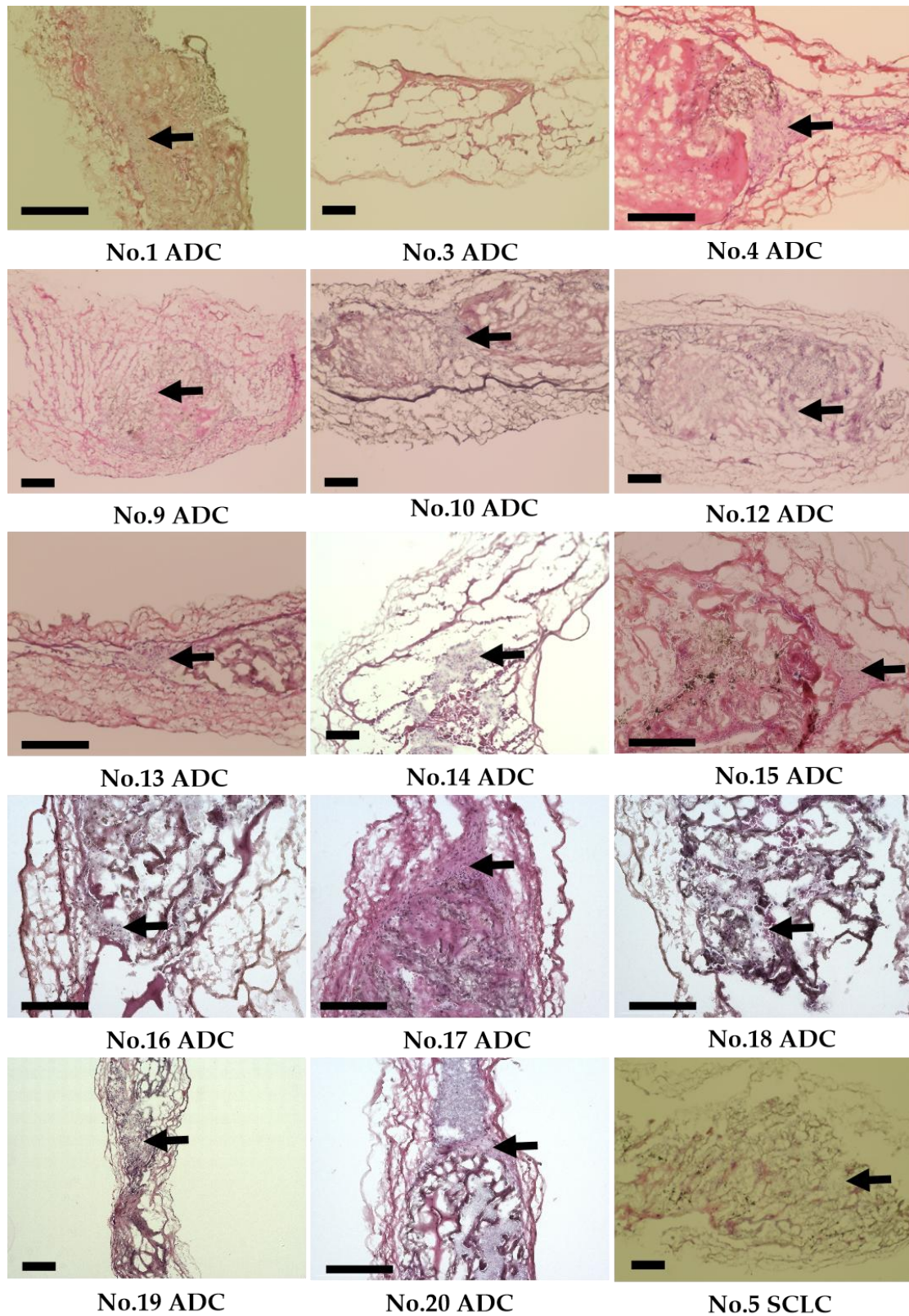No.19 ADC

No.20 ADC

No.5 SCLC

Figure 9. The morphology of adenocarcinoma lung cancer and small cell lung cancer 3D models.

HE stainings of static 3D sandwich models of patient number 1, 3-5, 9, 10, and 12-20. No.3 failed and there had no cells. SCLC: small cell lung cancer; ADC: adenocarcinoma. Black arrow: lung cancer cells. Scale bar = 200 µm.

4.4. Thickness and Cell Density of the Static 3D Model

In order to analyze cell growth in the static 3D model, we determined the tissue thickness and the cell density. We found no significant difference in the thickness at days 21 and 28 (570±183 µm vs 630±108 µm, p=0.0768) (Figure 10A). In the tumor area (ten-fold magnification), there was a higher cell density compared to the whole static 3D model (tiled images) irrespective of the analyzed time points (21 days, p < 0.001 or 28 days, p = 0.0116) (Figures 10 B,C). However, from day 21 to 28 the cell density increased from 613±204 cells/mm^2 to 887±259 cells/mm^2 (p =0.001) in the entire static 3D model (Figure 10D), while there was no significant cell density increase in the tumor area (p = 0.58) (Figure 10E). This suggests that during the fourth week of cultivation, the tumor cells proliferated mainly outside of the tumor piece area. However, the cultivation time of 21 and 28 days, respectively, was still not sufficient for the static 3D models to develop the same cell density as determined in the original tumor with 2873±473 cells/mm^2 (p < 0.001).
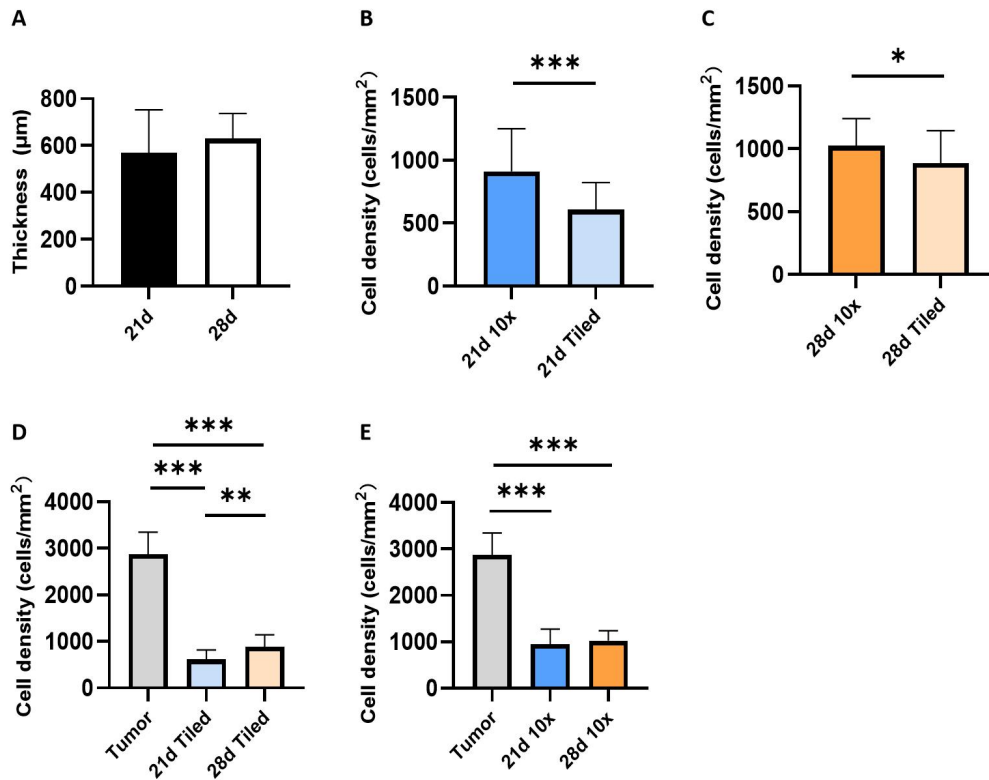
Figure 10. Thickness and cell density of the static 3D models.

(A) Tissue thickness at days 21 and 28. (B,C) Cell density at day 21 (B) and day 28 (C) determined by ten-fold magnification (10x) and tiled images, respectively. (D) Comparison of the cell density at 21 days and 28 days using tiled images (whole section) and (E) ten-fold magnification (10x) images (tumor area) with the original tumor. Significance was determined with the unpaired t-tests in A, B, and C and the one-way ANOVA and Tukey-test in D and E. Shown are the mean with standard deviation. n = 8, *: $p \leq 0.05$; **: $p \leq 0.01$; ***: $p \leq 0.001$.

4.5. The TME of the Static 3D Model

4.5.1. Identification of Lung Cancer Cells

In order to confirm the presence of lung cancer cells, we additionally performed immunofluorescence stainings against the specific lung cancer markers mentioned in the patient's clinical pathology reports. The tissue sections of the original tumor biopsies and the corresponding 3D model were

stained in parallel. Comparing the data of the pathology report (Table 15, see TTF-1/p63/p40 expression) with the staining results of the original tumor biopsies, in nine out of twelve tumor biopsies, the marker expression was consistent with the pathology report. Next, we compared the staining results of the original tumor biopsies with the corresponding 3D model. In ten different 3D models, we confirmed the presence/absence of the lung cancer marker analyzed in the 19 corresponding original tumor biopsies (Table 16). In tumor marker-positive 3D models, we detected single cells positive for TTF-1 (Figure 11) or p40/p63 (Figure 12), respectively, in the cancer colony with the lung cancer morphology. In the original tumor, cells showed heterogeneity of lung cancer markers, which was similar to the heterogeneous expression in static 3D models. The tumor pieces within the 3D models showed strong autofluorescence and cancer cells grew in and around the tumor pieces.

Table 16. List of lung cancer marker expression.

Number	Original tumor			3D model		
	TTF-1	p40	p63	TTF-1	p40	p63
1	-			-		
2		+			-	-
3	Failed, not detected			Failed, not detected		
4	-			-		
5	Not detected			Not detected		
6		+			-	-
7			+		-	+
8		+			-	-
9	+			-		
10	+			-		
11		+			+	

TTF-1/p63/p40 expression in the experiment				
12	-		-	
13	+		-	
14	-		-	
15	+		-	
16	+		+/-	
17	+		+/-	
18	+		-	
19	+		+	
20	-		-	
21	-	-	+	-

The expression of lung cancer markers. +: positive expression; -: negative expression; +/-: weak positive. Failed: The 3D model could not be established. Not detected: Patient number five was diagnosed as SCLC but TTF-1/p63/p40 expression was not detected.
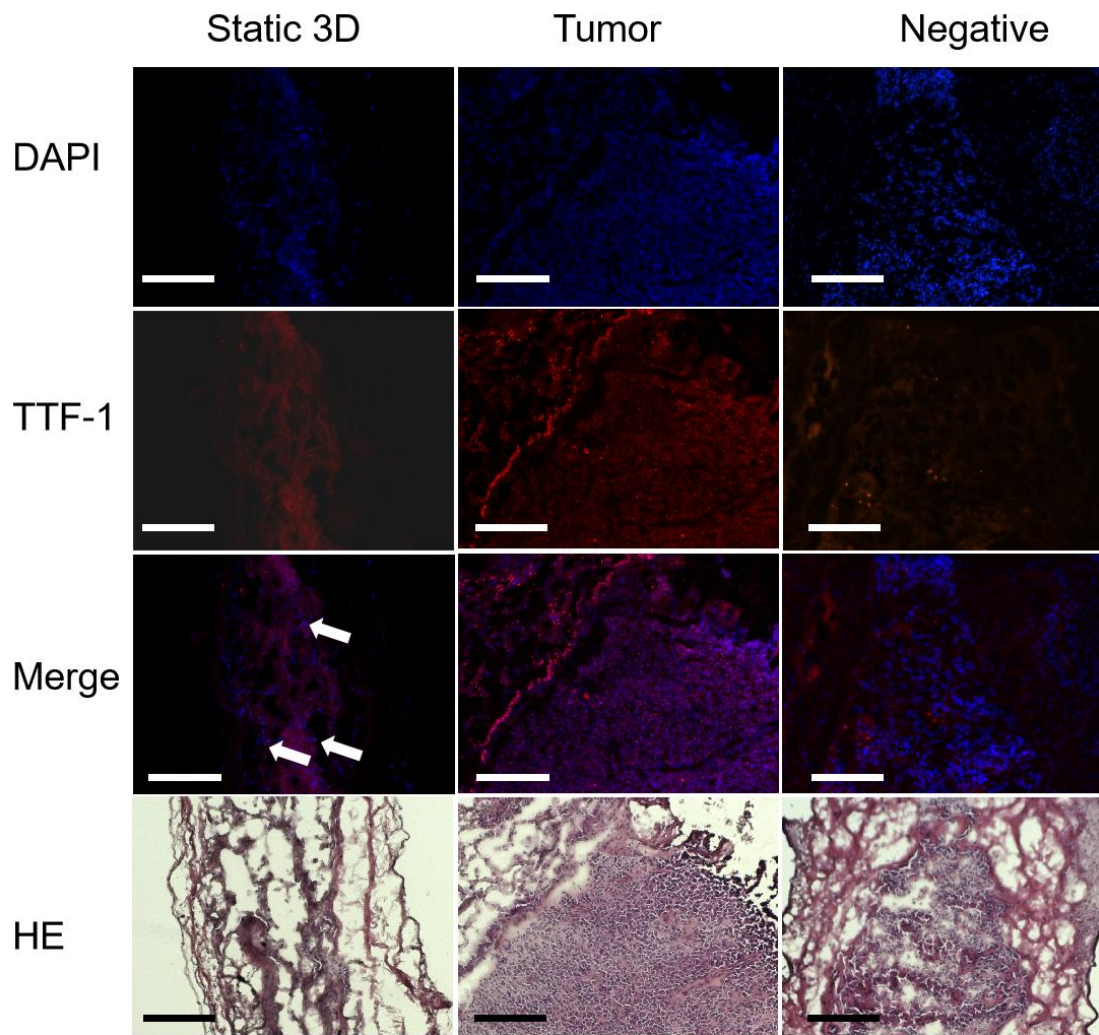
Figure 11. The expression of TTF-1 in the static 3D model and tumor biopsy.

The nuclei were stained with DAPI (blue) and the immunofluorescence staining against TTF-1 is displayed in orange color. The TTF-1-positive cells are purple colored in the merged photo (white arrows). The corresponding HE stainings showing the structures of the 3D models and morphology characteristics of the cells. As for negative control, the primary antibody was omitted. The scale bar represents 200 μm.

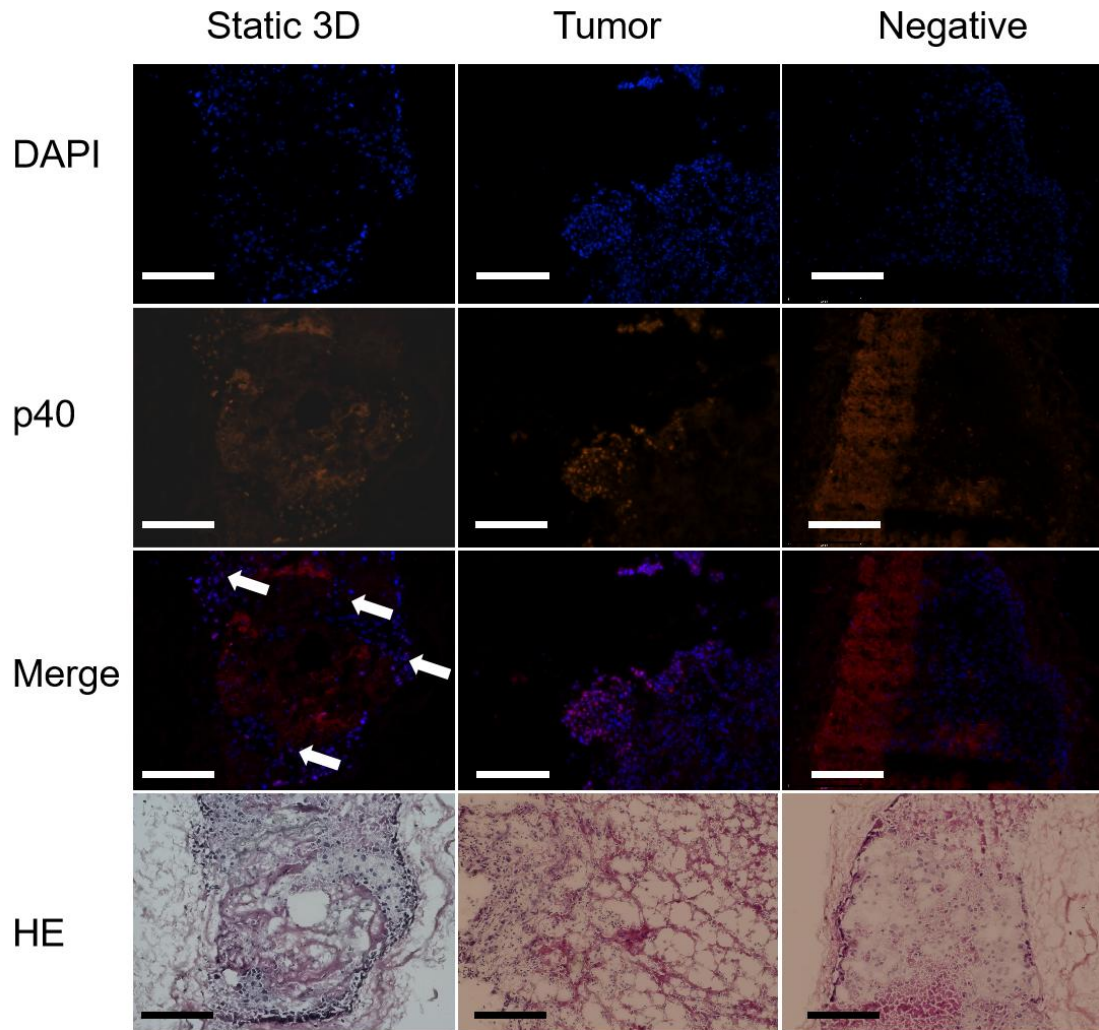|	Static 3D	Tumor	Negative
DAPI			
p40			
Merge			
HE			

Figure 12. The expression of p40 of the static 3D model and tumor.

The nuclei were stained with DAPI (blue) and the immunofluorescence staining against p40 is displayed in orange color. The p40-positive cells are purple colored in the merged photo (white arrows). The corresponding HE stainings showing the structures of the 3D models and morphology characteristics of the cells. As for negative control, the primary antibody was omitted. The scale bar represents 200 μm.

4.5.2. Identification of CAFs

As an important role of TME, CAFs interacted with tumor cells to promote the progression of tumor. We also detected CAFs in our static 3D models, which were identified by up-regulation of α-SMA and MCT4 in immunofluorescence staining. With the simultaneous presence of α-SMA and MCT4, we proved that

most CAFs assembled along the interface of tumor and matrix. Some CAFs grew within the matrix (Figure 13). In original tumor, most of α-SMA was highly expressed on vascular structure and mesenchymal tissue, while it was dispersively expressed in the static 3D model. In addition, the expression of MCT4 was less in original tumor than in the static 3D model.
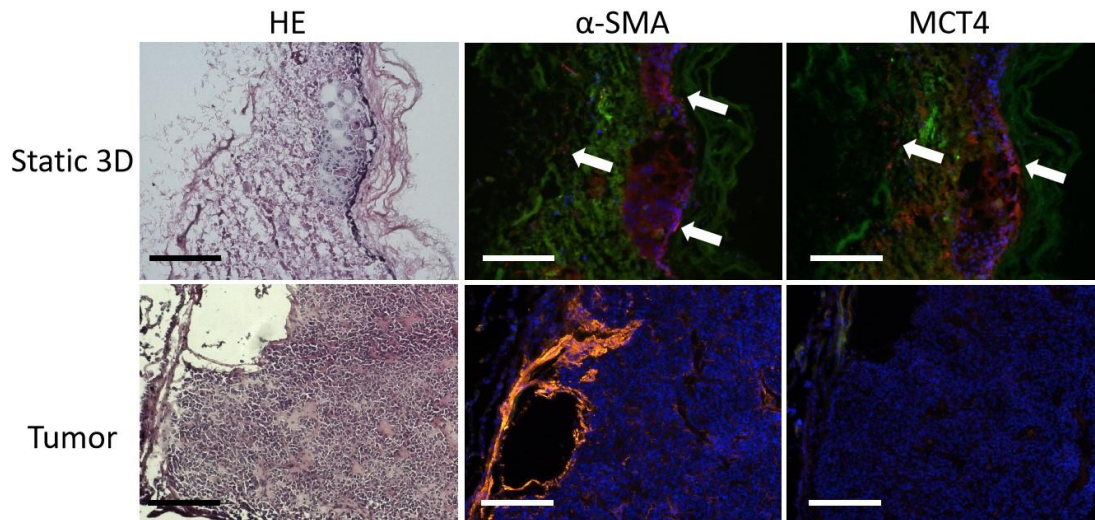

Figure 13. The expression of CAFs biomarkers in static 3D model and tumor. Immunofluorescence staining against α-SMA and MCT4 in orange color. In static 3D model, the positive cells are labeled with white arrows. Autofluorescence of the tumor and matrix accounts for the green fluorescence. The nuclei were stained with DAPI (blue). The corresponding HE stainings showing the structures of the 3D models and morphology characteristics of the cells. The scale bar represents 200 µm.

4.5.3. Identification of FN

Additionally, we verified the presence of fibronectin (FN) in our static 3D model, a component of the extracellular matrix (ECM), which supported the tumor cells in the TME. Strong FN signals were detected at the interface of tumor piece and matrix. The FN protein was found to fill the space between the tumor pieces and the matrix, extending along the latter (Figure 14). However, FN was less expressed within the tissue than at the edge of the section. The SIS matrix

surface and cutting processing could stimulate the tumor cells to produce FN. In summary, these findings suggest that lung cancer cells, CAFs, and the ECM component FN formed a TME in the static 3D model.
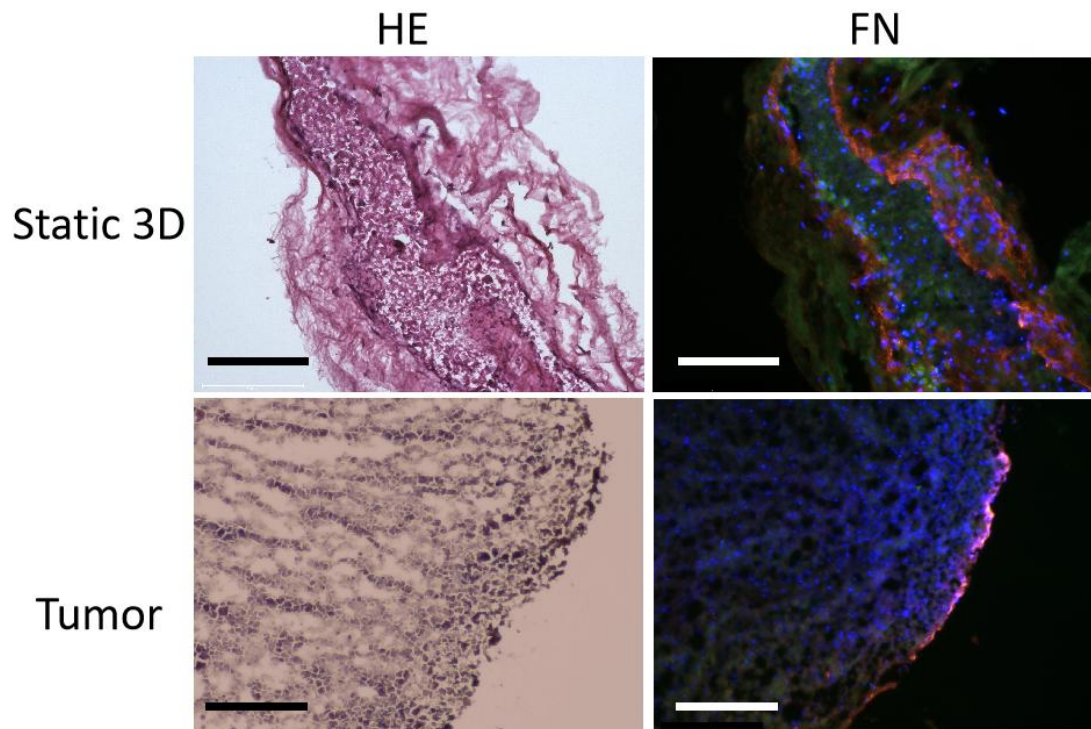

Figure 14. The expression of fibronectin (FN) in static 3D model and tumor. Immunofluorescence staining against fibronectin in orange color. Autofluorescence of the tumor and matrix accounts for green fluorescence. The nuclei were stained with DAPI (blue). The corresponding HE staining showed the structures of the 3D models and morphology characteristics of the cells. The scale bar represents 200 µm.

4.6. SISmuc Matrix in Static 3D Model

In our research group, the SISmuc matrix (Figure 15A), which possessed the mucosa layer and crypt structures which increases the contact area, was successfully applied for culture of lung tumor cell lines. Therefore, we also tested the SISmuc matrix in the static 3D cultivation with lung cancer cells. After 28 days of culture, tumor pieces and SISmuc matrix were detached from each other and there were no cellular structures found using the HE staining

(Figure 15B). With DAPI staining, we found no blue fluorescence signals from nuclei (Figure 15C-E). The mucosa layer and crypts were clearly presented in HE staining with protrusion structure and in DAPI staining with strong autofluorescence. The rare cells of this model suggested that SISmuc was not suitable to establish our lung cancer 3D model with original tumor pieces.
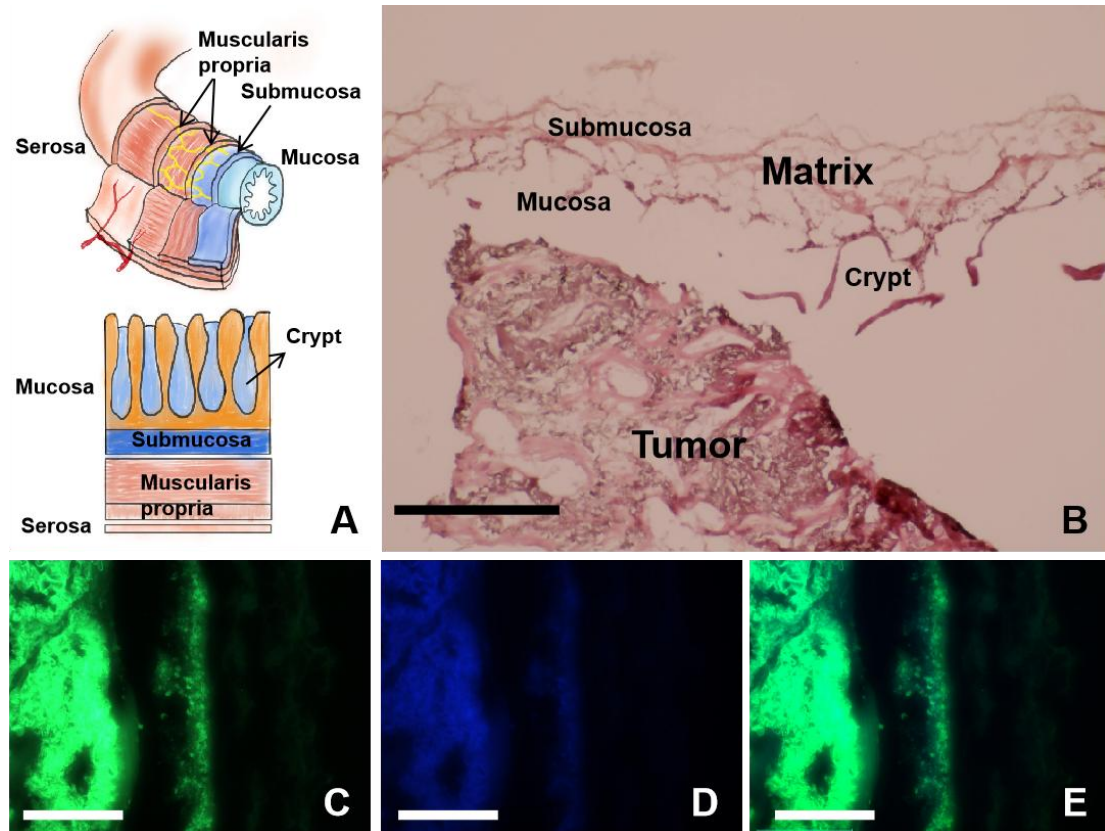

Figure 15. The static 3D model with SISmuc matrix.

The schema of intestine anatomic structure. Intestine included four main layers, and the crypt formed in the mucosa layer which enlarge the surface area. Modified by Microsoft. (B) HE staining of static 3D model with SISmuc. Tumor piece (without cells) detached from SISmuc matrix. (C-E) The DAPI staining of static 3D model with SISmuc matrix. (C) The autofluorescence of tumor and mucosa layer. (D) The nuclei were stained with DAPI (blue). (E) The merged photo showed nearly no cells stained with DAPI. The scale bar represents 200 μm in B and 100 μm in C-E.

4.7. Static 3D Models with Co-Cultivation

In order to support the growth of tumor cells in the 3D model, we tested two co-cultivation approaches with different types of fibroblasts. Fibroblasts are known to produce and to secrete growth factors and cytokines that support tumor cell growth. Therefore, we used 1) human primary bronchial fibroblasts (hbFb) and 2) mitotically inactivated NIH-3T3 cells. The latter have been already shown to support epithelial cell growth *in vitro* (Liu et al., 2012). Suboptimal culture conditions in turn have been shown to result in increased tumor cell apoptosis in *in vitro* culture models.

Therefore, we determined the epithelial cell specific apoptosis in the cell culture supernatants during the entire co-cultivation compared to the culture with the DMEM basal medium only. In the latter, we observed that the concentration of cck18 was significantly higher at 7 days and 14 days of cultivation compared to 28 days (Figure 16A). The cck18 concentration at 7 days was above 500 U/L (549.74±485.63) and decreased to 129.99±153.94 U/L at 28 days. There was no significant difference of the cck18 concentration comparing 28 days and day 0 ($p > 0.05$). This may indicate that after 28 days of culture a homeostasis was achieved resulting in almost no apoptosis.

The quantification of apoptosis in the medium of the hbFb co-culture showed a similar time course compared to the cultures with the DMEM medium (Figure 16B). At day 7, we detected the highest level of cck18 that decreased with time to 234.67±192.27 U/L at 28 days. However, in general, we measured higher cck18 concentrations compared to the DMEM cultured models. This suggested that the co-culture with hbFb was not as efficient as expected. In the second co-culture experiments, we utilized mitotically inactivated NIH-3T3 cells (Figure 16C). Here, the overall level of cck18 was below 200 U/L. The highest concentration was measured at days 7 and 14 which decreased to 159.49±104.30 U/L at 28 days and which was not significantly different from the negative control (day 0). These last data suggested that co-cultivation with

mitotically inactivated NIH-3T3 cells could support the tumor cell growth in the 3D model by reducing their apoptosis.
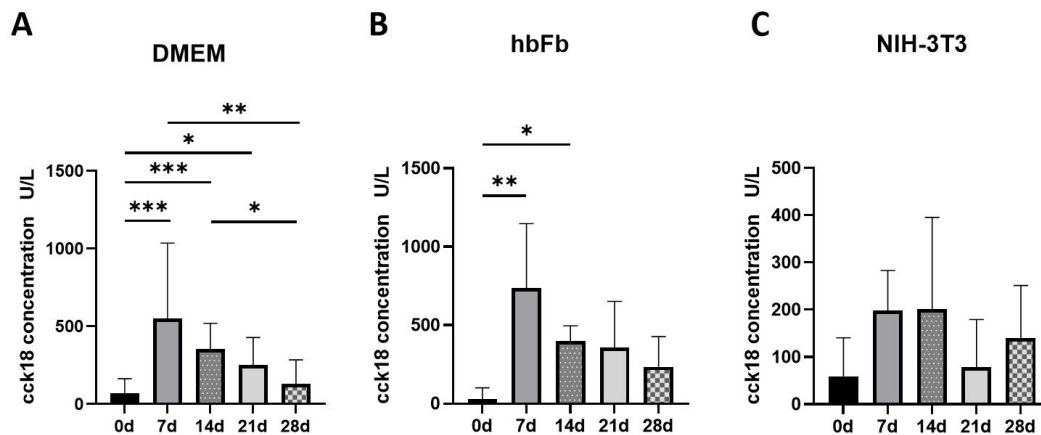

Figure 16. Measurement of apoptosis in the 3D model.

The cck18 concentration in the medium of static 3D culture with DMEM; n = 10 (A), in the medium of hbFb co-cultures; n=3 (B), and in the medium of NIH-3T3 co-cultures; n=4 (C). Statistical significance was determined using the Kruskal-Wallis test and Dunn's multiple comparisons test. Shown are the mean with standard deviation. *: p ≤ 0.05; **: p ≤ 0.01; ***: p ≤ 0.001.

4.8. Morphological Features of Dynamic 3D Culture Model

In addition to the co-cultivation approach, we tested whether continuous flow of the culture medium supports cell growth in the 3D model. For this, we applied a constant medium flow of 1.5 mL/min that has been shown earlier to be suitable for the bioreactor used. After 28 days of dynamic culture, the 3D lung cancer model showed obvious complexity of morphology structures in the HE staining. In general, dynamic 3D model possessed the same "sandwich" structure as the static 3D model, including two layers of matrix and tumor pieces. However, the edge of tumor- tumor pieces and tumor- SIS matrix became indistinct and the whole 3D model showed overall growth (Figure 17). Different cell colonies were connected with ECM and kept their own

morphological features, such as intercellular bridge and nuclear-cytoplasmic ratio. The tiled image shows that some cell colonies could form not only within the tumor pieces, but also on the outer surface of the matrix.
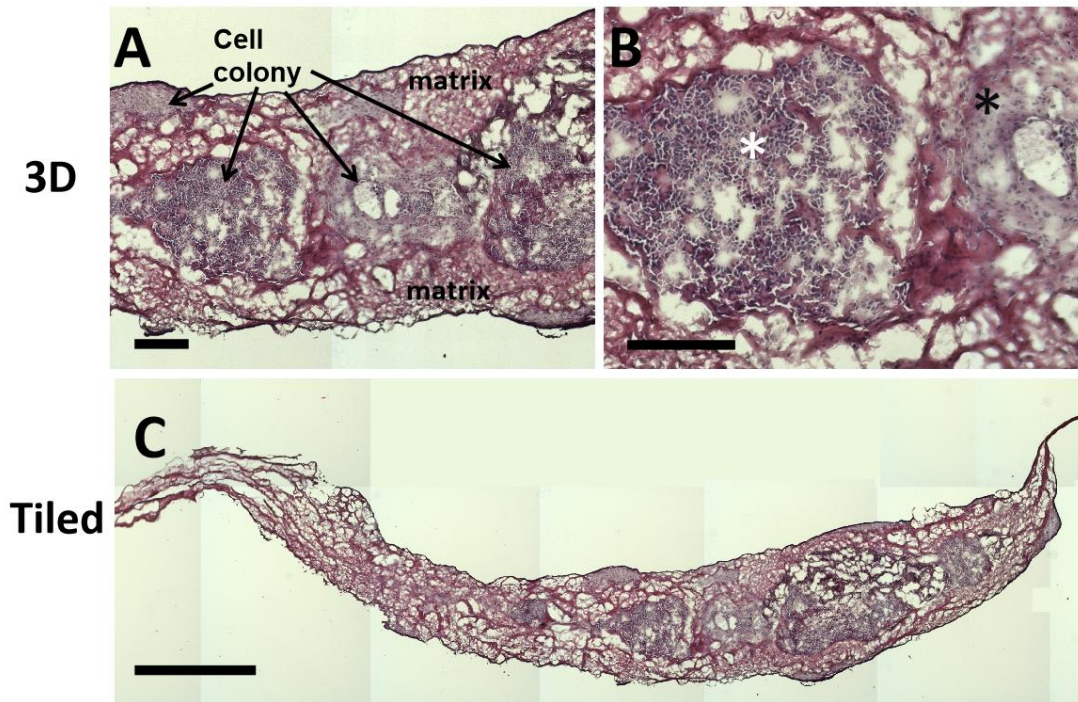

Figure 17. Morphology of dynamic 3D model.

(A) The "sandwich" structure of dynamic 3D model using HE staining. Two layers of SIS matrix covered the tumor pieces. (B) Different cell colony possessed different morphological features. One cell colony had intercellular bridges (white star), while the nearby colony had no intercellular bridges (black star). (C) The tiled image of dynamic 3D model. Scale bar represents 200 µm in A ,B and 1000 µm in C.

4.9. Comparison of the Static 3D Model with the Dynamic 3D Model

In order to directly compare the static and dynamic cultivation, static and dynamic 3D models of the same tumor biopsy were cultivated in parallel for 28 days with the DMEM basal medium and the thickness and cell density were measured to analyze the growth of the 3D models. The dynamic 3D models

were thicker than the static 3D model (925±256 µm vs 522±78 µm, p < 0.001), suggesting more favorable growth conditions in the dynamic cultivation system (Figure 18A). In accordance with our previous findings, tumor pieces only (see static 3D 10x and dynamic 3D 10x) had a higher cell density than the cell density of whole sample (see static 3D tiled and dynamic 3D tiled) both in the static 3D model (p < 0.001, Figure 18B) and the dynamic 3D model (p = 0.0026, Figure 18C). In the tiled images, the cell density of the dynamic 3D model was higher compared to the static 3D model with 1470±220 cells/mm^2 and 956±118 cells/mm^2, respectively (p =0.0086, Figure 18D). The ten-fold magnification images also confirmed that the cell density of dynamic 3D model was higher than in the static 3D model (1961±533 vs 1345±231 cells/mm^2, p =0.0091) (Figure 18E). These data suggested that the dynamic 3D models grew faster than the corresponding static 3D model within 28 days of cultivation. Although cell densities of the 3D models were lower than in the original tumor (3487±736 cells/mm^2), the dynamic 3D model showed higher cell density than the static 3D model, especially in the tumor pieces area.
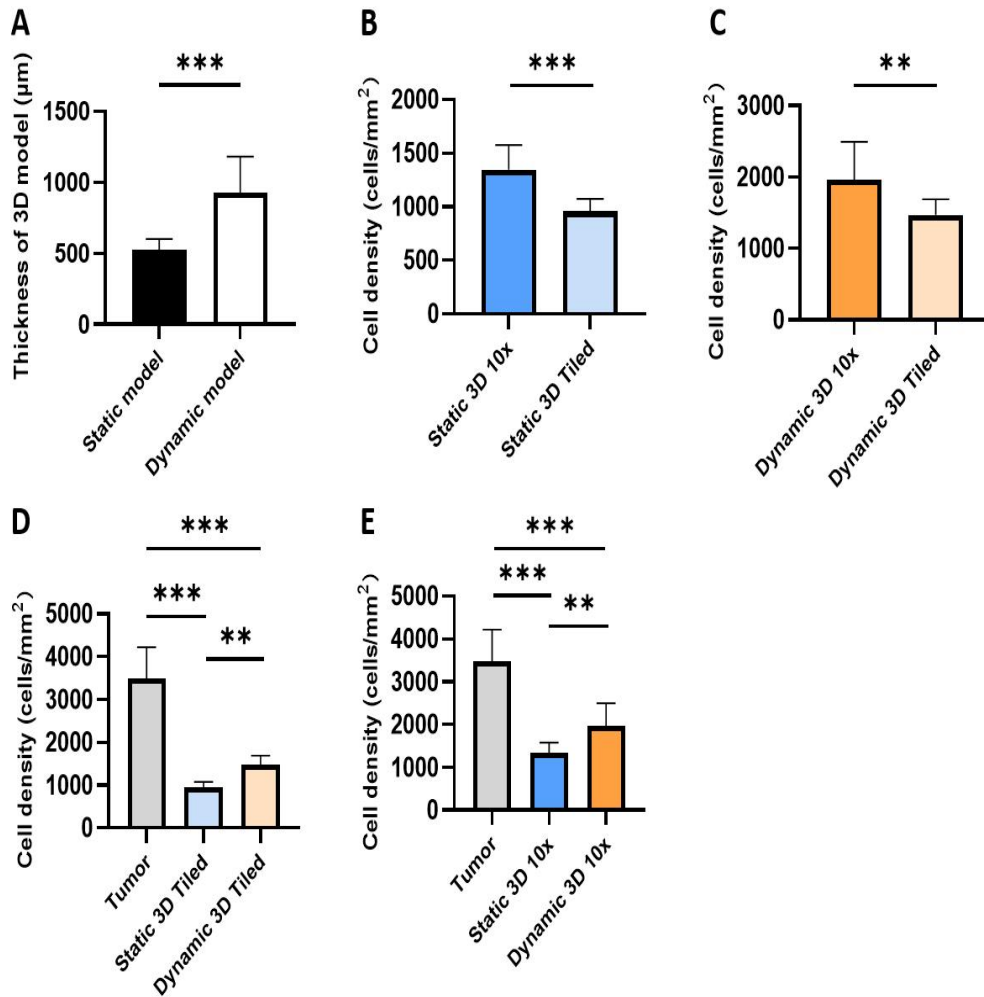
Figure 18. Comparison of the static and the dynamic 3D model.

(A) Thickness of the static and the dynamic 3D model at 28 days. (B) Cell density of the static 3D model in ten-fold magnification (tumor area) and tiled images (whole section). (C) Cell density of the dynamic 3D model in ten-fold magnification and tiled images. (D) Comparison between static and dynamic 3D models with tiled image. (E) The comparison between static and dynamic 3D models with ten-fold magnification image. Statistical significance was determined using the Mann-Whitney U tests in A, unpaired t-test in B and C, and one-way ANOVA and Tukey-test in D and E. Shown are the mean with standard deviation. n = 3, *: $p \leq 0.05$; **: $p \leq 0.01$; ***: $p \leq 0.001$.

5. Discussion

In order to further investigate the progression of lung cancer, scientists established both *in vivo* and *in vitro* models of lung cancer in recent years. In this thesis, we explored a new method for establishing an *in vitro* 3D lung cancer model with small intestinal submucosa scaffold. After optimizing the cultivation conditions, the static 3D model showed a higher success rate than 2D model and possessed primary tumor microenvironment. In addition, the dynamic medium system supported high nutrition for 3D model which possessed higher cell density.

5.1. The Success Rate of *In Vitro* Lung Cancer Models

After 28 days of cultivation, our 3D model showed a higher success rate than the corresponding 2D model with 94% and 19%, respectively. In contrast, organoids from NSCLC showed a low establishment rate of only 17% (Dijkstra et al., 2020). These *in vitro* models lack the original TME that is known to influence the proliferation of tumor cells (Aguirre-Ghiso et al., 2001). In addition, there is a lack of molecular interaction between different types of cells. To circumvent these limitations, we used primary lung tumor pieces and a biological collagen matrix to establish a new *in vitro* 3D lung tumor model. This allowed us to maintain not only the tumor cells but also other cells in a spatial structure of the TME.

According to different research goals, the criteria of success rate of 3D models vary between groups. In the field of human tissue replacement where a high in vitro/in vivo correlation is intended, the 3D model is expected to possess more original structures and components. However, for high-throughput drug screening an uncomplicated culture system, low cost, and small size of 3D models are required for the success cases (Shamir & Ewald, 2014). In the present research work, keeping the original tumor microenvironment as much as possible was an important goal. Therefore, the criterion of success case in my research required two or more different cell types existing in the in vitro model.

58

The success cases of the 3D models were identified by morphological features and the 3D model which contained epithelial cell-like tissue were regarded as success case (Kim et al., 2019). The authors of Kim et al. divided the cells of their 3D model into epithelial cell-like, fibroblast cell-like and no cell according to their experience and morphological shape of the tissue. In addition, the functional characteristic of 3D models could become a criterion, for example the expression of immune checkpoint biomarker in 3D models (Jenkins et al., 2018).

5.2. The Identification of Tumor Cells in the 3D Model

In the 3D model, we found tumor pieces which maintained a part of the original tumor morphology. Adenocarcinoma possessed flat, cohesive sheets of rather uniform appearing glandular cells and the squamous cell carcinoma exhibited intercellular bridges as described earlier (Travis et al., 2013). Fibroblast cells and tumor cells had different spatial distribution with fibroblasts surrounding cancer colonies and migrating into the matrix. However, cells in 2D lung cancer models lacked the spatial distribution and the cell to matrix interaction, which was found to be required for maintaining cellular functions and defining phenotypes of lung cancer (Zhang et al., 2018).

Besides the tumor cells morphology, the tumor markers play an important role in the diagnosis of the lung cancer. Previous pathology research reported that the majority of SQCC and ADC (56%) can be identified with cytomorphology alone (Kimbrell et al., 2012) and 38% of samples can be identified with extra immune staining (Zakowski et al., 2016). Therefore, we utilized histological method and immunostainings for the determination and characterization of the tumor cells in the 3D model. For immunostainings, we used the most common lung cancer markers TTF-1 for ADC and p40/p63 for SQCC according to the corresponding pathology report. In the 3D model compared to the original tumor biopsy, we confirmed the absence/presence of the tumor marker for 10 out of 19 cases. But the immunostainings demonstrated strong heterogeneity,

because only few single cells were positive for the tumor markers. This could be due to the downregulation of marker expression during *in vitro* cultivation. Another reason could be a selection for specific cell types or outgrowth of non-malignant cells.

5.3. The TME of 3D Model

In the static 3D model, the existence of the tumor microenvironment including cancer associated fibroblasts and fibronectin was shown. Fibroblasts positive for α-SMA and MCT4 were considered to be CAFs (Kalluri, 2016; Martinez-OutschoornSotgia & Lisanti, 2014). Catabolic CAFs (MCT4-positive) are known to play an important role in enabling cancer cell propagation, survival, and systemic dissemination during metastasis (Martinez-Outschoorn et al., 2014). In the static 3D model, these two markers were expressed at the same location in the same type of cells which were identified by corresponding HE staining. This suggested that CAFs existed and played a role in supporting the survival of cancer cells in the static 3D model.

According to previous research, FN is primarily synthesized by CAFs and deposits into the ECM that acts as scaffold for molecules such as growth factors and cell surface receptors (Pankov & Yamada, 2002). Due to the same distribution of FN and CAFs on the interface of cancer colony and matrix, we hypothesize that the linear FN was produced by the CAFs in the static 3D model. In the stroma of NSCLC, FN was found to be overexpressed and promoted cancer cell adhesion, growth, differentiation, migration, invasion, survival, and resistance to chemotherapy (Spada, Tocci, Di Modugno, & Nisticò, 2021).

Due to distinct goals of the investigations, CAFs and other cells were regarded as an important cause of failure during cultivation of cancer organoids and various techniques were implemented to inhibit the outgrowth of normal cells (Weeber, Ooft, Dijkstra, & Voest, 2017) (Drost & Clevers, 2018). However, we

preserved not only cancer cells but also other original cells and extracellular matrix, which combined with the SIS matrix formed the main TME of our 3D model. With the presence of CAFs and FN, therefore, our 3D model could be used for drug testing targeting CAFs and adjacent stroma.

5.4. Cultivation of 3D Model

5.4.1. Simple Medium Composition

The culture medium of the 3D model may also play an important role for cell growth and death. We cultured the 3D model with simple composition, which included 10% of FCS and 1% of antibiotics in DMEM. This may support the essential nutrition for proliferation and limit the contamination of bacteria and fungi which are located in the original lung tissue. However, in previous research, media with complex composition were used for *in vitro* models for the purposes of stimulating high proliferation and selection of a high purity cell group. The supplementation with the Rho kinase (ROCK) inhibitor compound, Y-2763, has been shown to minimize also cell death and to increase organoid outgrowth (DriehuisKretzschmar & Clevers, 2020).

In addition, the B27 supplement which was designed for supporting proliferation of neural cells was commonly supplemented in the medium for organoids from different organs. The B27 supplement was created for hippocampal neurons cultivation and it allows the neural cell cultivation in glia cell free environment with long-term viability (Brewer, Torricelli, Evege, & Price, 1993). Moreover, Nutlin-3a was used to get a high purity of tumor cells with TP53 mutation and induced the cell death of p53 wild type normal cells (Kucab, Hollstein, Arlt, & Phillips, 2017), Although various of supplements had been added in cultivation media, the concentration and specific mechanism in different organoid cultures are still unclear.

In our 3D model, we kept the TME from the tumor including different original cells and matrix that could also support the growth of the cells. In future

experiments, however, we could also test the influence of the ROCK inhibitor with the purpose of reducing the loss of cells during the preparing process and improving the cultivation medium.

5.4.2. Co-Culture System

In this study, a co-culture technique was used to improve the culture conditions and to promote the generation of the *in vitro* model. Two different cell types, hbFb and mitotically inactivated NIH-3T3 cells, were used for the co-culture with the static 3D model. The fibroblasts interacted with the 3D model through the medium which was an indirect communication. In the static 3D model with DMEM medium and with hbFb co-culture, the apoptosis during the first two weeks was high which then decreased to amounts lower than 200 U/L. However, co-culture with mitotically inactivated NIH-3T3 cells resulted in constantly low apoptosis which may support the growth of the tumor cells.

For co-culltivation, cells of different origin, such as tumor tissue with adjacent normal tissue, highly differentiated cells with pluripotent stem cells, as well as human cells and other species cells have been used (Shamir et al., 2014). NIH-3T3 cells have been co-cultured with not only normal cells but also cancer cells, and they improved the proliferation, growth, and attachment of co-cultured cancer cells by producing diffusible factors, growth factors, and extracellular matrix (Liu et al., 2020). In our co-culture system, the NIH-3T3 cells may supported the tumor cells and significantly reduced the cell death from the first week of cultivation with a low apoptosis level.

5.4.3. Dynamic Medium Supply System

To improve the medium supply and metabolic waste transfer, we established the dynamic 3D model. Compared to the static 3D model, the dynamic 3D model was thicker and possessed higher cell density after 28 days cultivation. These results were similar to the results of the dynamic cultivation with human

mesenchymal stem cells in another research group (REF). After four weeks of cultivation, they found that in their dynamic 3D model not only more cells existed but also more extracellular matrix was produced with higher staining ratio, compared to static models and spinner flask model which had constantly medium stirred up by spinner (Tsai, Yang, Wu, Chen, & Tseng, 2019).

Similar to the results of the static 3D model, the tumor pieces area still showed the highest cell density compared to the whole area of dynamic 3D model section. These suggested that tumor pieces played a role of a germinal center in the 3D model and the whole area of 3D model still had space for more cells with higher cell density. Compared to the static culture, the dynamic culture improved the speed of nutrition exchange and removing of tissue metabolism byproducts through the constant medium fluid. But, the fluid shear stress could induce morphology changes and epithelial mesenchymal transition process with different phenotypic distribution (Liu et al., 2016). However, our 3D model had two layers of SIS matrix which cover the tumor pieces outside that maybe prevent the cells from shear stress of the medium fluid. With sufficient medium supporting and growth space, our 3D model has the potential for long-term culture (more than 3 months) (Shi et al., 2020).

6. Outlook

In future experiments, we plan to gradually prolong the cultivation time for the 3D model to reach a higher cell density. In addition, we intend to use magnetic resonance spectroscopy to analyse the metabolism of our 3D model, which is used in the clinic as a non-invasive method for solid tumor diagnosis.

7. Conclusion

We established a new 3D *in vitro* lung cancer model simulating the TME for 28 days. The 3D model showed a higher success rate and structural complexity

than 2D models, which makes them suitable for future translational and oncological research.

8. Reference

Aguirre-Ghiso, J. A., Liu, D., Mignatti, A., Kovalski, K., & Ossowski, L. 2001. Urokinase receptor and fibronectin regulate the ERK(MAPK) to p38(MAPK) activity ratios that determine carcinoma cell proliferation or dormancy in vivo. Mol Biol Cell, 12(4): 863-879.

Alexander, J. & Cukierman, E. 2016. Stromal dynamic reciprocity in cancer: intricacies of fibroblastic-ECM interactions. Curr Opin Cell Biol, 42: 80-93.

American Cancer Society, A. 2020. American Cancer Society. Lung cancer survival rates: 5-year relative survival rate.

Aros, C. J. & Pantoja, C. J. & Gomperts, B. N. 2021. Wnt signaling in lung development, regeneration, and disease progression. Commun Biol, 4(1): 601.

Badylak, S., Liang, A., Record, R., Tullius, R., & Hodde, J. 1999. Endothelial cell adherence to small intestinal submucosa: an acellular bioscaffold. Biomaterials, 20(23-24): 2257-2263.

Barkan, D., Kleinman, H., Simmons, J. L., Asmussen, H., Kamaraju, A. K., Hoenorhoff, M. J., Liu, Z. Y., Costes, S. V., Cho, E. H., Lockett, S., Khanna, C., Chambers, A. F., & Green, J. E. 2008. Inhibition of metastatic outgrowth from single dormant tumor cells by targeting the cytoskeleton. Cancer Res, 68(15): 6241-6250.

Barkan, D., El, T. L., Michalowski, A. M., Smith, J. A., Chu, I., Davis, A. S., Webster, J. D., Hoover, S., Simpson, R. M., Gauldie, J., & Green, J. E. 2010. Metastatic growth from dormant cells induced by a col-I-enriched fibrotic environment. Cancer Res, 70(14): 5706-5716.

Bishop, J. A. & Sharma, R. & Illei, P. B. 2010. Napsin A and thyroid transcription factor-1 expression in carcinomas of the lung, breast, pancreas, colon, kidney, thyroid, and malignant mesothelioma. Hum Pathol, 41(1): 20-25.

Brewer, G. J., Torricelli, J. R., Evege, E. K., & Price, P. J. 1993. Optimized survival of hippocampal neurons in B27-supplemented Neurobasal, a new serum-free medium combination. J Neurosci Res, 35(5): 567-576.

Broutier, L., Mastrogiovanni, G., Verstegen, M. M., Francies, H. E., Gavarró, L. M., Bradshaw, C. R., Allen, G. E., Arnes-Benito, R., Sidorova, O., Gaspersz, M. P., Georgakopoulos, N., Koo, B. K., Dietmann, S., Davies, S. E., Praseedom, R. K., Lieshout, R., IJzermans, J., Wigmore, S. J., Saeb-Parsy, K., Garnett, M. J., van der Laan, L. J., & Huch, M. 2017. Human primary liver cancer-derived organoid cultures for disease modeling and drug screening. Nat Med, 23(12): 1424-1435.

Casarin, M., Fortunato, T. M., Imran, S., Todesco, M., Sandrin, D., Borile, G., Toniolo, I., Marchesan, M., Gerosa, G., Bagno, A., Romanato, F., Carniel, E. L., Morlacco, A., & Dal Moro, F. 2022. Porcine Small Intestinal Submucosa (SIS) as a Suitable Scaffold for the Creation of a Tissue-Engineered Urinary Conduit: Decellularization, Biomechanical and Biocompatibility Characterization Using New Approaches. Int J Mol Sci, 23(5).

Chan, R. K., Zamora, D. O., Wrice, N. L., Baer, D. G., Renz, E. M., Christy, R. J., & Natesan, S. 2012. Development of a vascularized skin construct using adipose-derived stem cells from debrided burned skin. Stem Cells Int, 2012: 841203.

Chhabra, Y. & Weeraratna, A. T. 2023. Fibroblasts in cancer: Unity in heterogeneity. Cell, 186(8): 1580-1609.

Cui, W., Yang, L., Ullah, I., Yu, K., Zhao, Z., Gao, X., Liu, T., Liu, M., Li, P., Wang, J., & Guo, X. 2022. Biomimetic porous scaffolds containing decellularized small intestinal submucosa and $Sr(2+)/Fe(3+)$co-doped hydroxyapatite accelerate angiogenesis/osteogenesis for bone regeneration. Biomed Mater, 17(2).

de Visser, K. E. & Joyce, J. A. 2023a. The evolving tumor microenvironment: From cancer initiation to metastatic outgrowth. Cancer Cell, 41(3): 374-403.

de Visser, K. E. & Joyce, J. A. 2023b. The evolving tumor microenvironment: From cancer initiation to metastatic outgrowth. Cancer Cell, 41(3): 374-403.

Di Martino, J. S., Nobre, A. R., Mondal, C., Taha, I., Farias, E. F., Fertig, E. J., Naba, A., Aguirre-Ghiso, J. A., & Bravo-Cordero, J. J. 2022. A tumor-derived type III collagen-rich ECM niche regulates tumor cell dormancy. <u>Nat Cancer</u>, 3(1): 90-107.

Di Modugno, F., Spada, S., Palermo, B., Visca, P., Iapicca, P., Di Carlo, A., Antoniani, B., Sperduti, I., Di Benedetto, A., Terrenato, I., Mottolese, M., Gandolfi, F., Facciolo, F., Chen, E. I., Schwartz, M. A., Santoni, A., Bissell, M. J., & Nisticò, P. 2018. hMENA isoforms impact NSCLC patient outcome through fibronectin/β1 integrin axis. <u>Oncogene</u>, 37(42): 5605-5617.

Dijkstra, K. K., Monkhorst, K., Schipper, L. J., Hartemink, K. J., Smit, E. F., Kaing, S., de Groot, R., Wolkers, M. C., Clevers, H., Cuppen, E., & Voest, E. E. 2020. Challenges in Establishing Pure Lung Cancer Organoids Limit Their Utility for Personalized Medicine. <u>Cell Reports</u>, 31(5): 107588.

Dong, X., Guan, J., English, J. C., Flint, J., Yee, J., Evans, K., Murray, N., Macaulay, C., Ng, R. T., Gout, P. W., Lam, W. L., Laskin, J., Ling, V., Lam, S., & Wang, Y. 2010. Patient-derived first generation xenografts of non-small cell lung cancers: promising tools for predicting drug responses for personalized chemotherapy. <u>Clin Cancer Res</u>, 16(5): 1442-1451.

Dong, Y., Liu, Z., Qi, F., Jin, L., Zhang, L., & Zhu, N. 2019. Polyethylene-Glycol-Ornamented Small Intestinal Submucosa Biosponge for Skin Tissue Engineering. <u>ACS Biomater Sci Eng</u>, 5(5): 2457-2465.

Driehuis, E. & Kretzschmar, K. & Clevers, H. 2020. Establishment of patient-derived cancer organoids for drug-screening applications. <u>Nature Protocols</u>, 15(10): 3380-3409.

Drost, J. & Clevers, H. 2018. Organoids in cancer research. <u>Nat Rev Cancer</u>, 18(7): 407-418.

Du Y, Li, X., Niu, Q., Mo, X., Qui, M., Ma, T., Kuo, C. J., & Fu, H. 2020. Development of a miniaturized 3D organoid culture platform for ultra-high-throughput screening. <u>J Mol Cell Biol</u>, 12(8): 630-643.

Duma, N. & Santana-Davila, R. & Molina, J. R. 2019. Non-Small Cell Lung Cancer: Epidemiology, Screening, Diagnosis, and Treatment. <u>Mayo Clin Proc</u>, 94(8): 1623-1640.

Evison, M. 2020. The current treatment landscape in the UK for stage III NSCLC. <u>Br J Cancer</u>, 123(Suppl 1): 3-9.

Feeley, B. T., Liu, N. Q., Conduah, A. H., Krenek, L., Roth, K., Dougall, W. C., Huard, J., Dubinett, S., & Lieberman, J. R. 2006. Mixed metastatic lung cancer lesions in bone are inhibited by noggin   overexpression and Rank:Fc administration. <u>J Bone Miner Res</u>, 21(10): 1571-1580.

Frese, K. K. & Simpson, K. L. & Dive, C. 2021. Small cell lung cancer enters the era of precision medicine. <u>Cancer Cell</u>, 39(3): 297-299.

Frost, N., Griesinger, F., Hoffmann, H., Länger, F., Nestle, U., Schütte, W., Wolf, J., & Reck, M. 2022. Lung Cancer in Germany. <u>J Thorac Oncol</u>, 17(6): 742-750.

Ge, H., Cheng, N., Xu, X., Yang, Z., Hoffman, R. M., & Zhu, J. 2019. AMMECR1 Inhibits Apoptosis and Promotes Cell-cycle Progression and Proliferation   of the A549 Human Lung Cancer Cell Line. <u>Anticancer Res</u>, 39(9): 4637-4642.

Ghaedi, M. & Niklason, L. E. & Williams, J. 2015. Development of Lung Epithelium from Induced Pluripotent Stem Cells. <u>Curr Transplant Rep</u>, 2(1): 81-89.

Guo, H. & Bai, R. & Cui, J. 2020. [Advances in Combination Therapy of Immune Checkpoint Inhibitors for Lung   Cancer]. <u>Zhongguo Fei Ai Za Zhi</u>, 23(2): 101-110.

Gurda, G. T., Zhang, L., Wang, Y., Chen, L., Geddes, S., Cho, W. C., Askin, F., Gabrielson, E., & Li, Q. K. 2015. Utility of five commonly used immunohistochemical markers TTF-1, Napsin A, CK7,   CK5/6 and P63 in primary and metastatic adenocarcinoma and squamous cell   carcinoma of the lung: a retrospective study of 246 fine needle aspiration cases. <u>Clin Transl Med</u>, 4: 16.

He, S., Lu, Y., Liu, X., Huang, X., Keller, E. T., Qian, C. N., & Zhang, J. 2015. Wnt3a: functions and implications in cancer. <u>Chin J Cancer</u>, 34(12): 554-562.

Herreros-Pomares, A., Zhou, X., Calabuig-Fariñas, S., Lee, S. J., Torres, S., Esworthy, T., Hann, S. Y., Jantus-Lewintre, E., Camps, C., & Zhang, L. G. 2021. 3D printing novel in

vitro cancer cell culture model systems for lung cancer stem   cell study. Mater Sci Eng C Mater Biol Appl, 122: 111914.

Hoppensack, A., Kazanecki, C. C., Colter, D., Gosiewska, A., Schanz, J., Walles, H., & Schenke-Layland, K. A human in vitro model that mimics the renal proximal tubule., 20(7): 599-609.

Hosseinirad, H., Rashidi, M., Moghaddam, M. M., Tebyanian, H., Nouraei, S., Mirhosseini, S. A., Rasouli, M., & Habibian, S. 2018. Stem cell therapy for lung diseases: From fundamental aspects to clinical   applications. Cell Mol Biol (Noisy-le-grand), 64(10): 92-101.

Hsu, Y. L., Hung, J. Y., Chang, W. A., Jian, S. F., Lin, Y. S., Pan, Y. C., Wu, C. Y., & Kuo, P. L. 2018. Hypoxic Lung-Cancer-Derived Extracellular Vesicle MicroRNA-103a Increases the   Oncogenic Effects of Macrophages by Targeting PTEN. Mol Ther, 26(2): 568-581.

Huang, J., Zhang, L., Wan, D., Zhou, L., Zheng, S., Lin, S., & Qiao, Y. 2021. Extracellular matrix and its therapeutic potential for cancer treatment. Signal Transduct Target Ther, 6(1): 153.

Hussey, G. S. & Keane, T. J. & Badylak, S. F. 2017. The extracellular matrix of the gastrointestinal tract: a regenerative medicine   platform. Nat Rev Gastroenterol Hepatol, 14(9): 540-552.

Jainchill, J. L. & Aaronson, S. A. & Todaro, G. J. 1969. Murine sarcoma and leukemia viruses: assay using clonal lines of   contact-inhibited mouse cells. J Virol, 4(5): 549-553.

Jannasch, M., Groeber, F., Brattig, N. W., Unger, C., Walles, H., & Hansmann, J. 2015. Development and application of three-dimensional skin equivalents for the investigation of percutaneous worm invasion. Experimental Parasitology, 150: 22-30.

Jenkins, R. W., Aref, A. R., Lizotte, P. H., Ivanova, E., Stinson, S., Zhou, C. W., Bowden, M., Deng, J., Liu, H., Miao, D., He, M. X., Walker, W., Zhang, G., Tian, T., Cheng, C., Wei, Z., Palakurthi, S., Bittinger, M., Vitzthum, H., Kim, J. W., Merlino, A., Quinn, M., Venkataramani, C., Kaplan, J. A., Portell, A., Gokhale, P. C., Phillips, B., Smart, A., Rotem, A., Jones, R. E., Keogh, L., Anguiano, M., Stapleton, L., Jia, Z., Barzily-Rokni,

M., Cañadas, I., Thai, T. C., Hammond, M. R., Vlahos, R., Wang, E. S., Zhang, H., Li, S., Hanna, G. J., Huang, W., Hoang, M. P., Piris, A., Eliane, J. P., Stemmer-Rachamimov, A. O., Cameron, L., Su, M. J., Shah, P., Izar, B., Thakuria, M., LeBoeuf, N. R., Rabinowits, G., Gunda, V., Parangi, S., Cleary, J. M., Miller, B. C., Kitajima, S., Thummalapalli, R., Miao, B., Barbie, T. U., Sivathanu, V., Wong, J., Richards, W. G., Bueno, R., Yoon, C. H., Miret, J., Herlyn, M., Garraway, L. A., Van Allen, E. M., Freeman, G. J., Kirschmeier, P. T., Lorch, J. H., Ott, P. A., Hodi, F. S., Flaherty, K. T., Kamm, R. D., Boland, G. M., Wong, K. K., Dornan, D., Paweletz, C. P., & Barbie, D. A. 2018. Ex Vivo Profiling of PD-1 Blockade Using Organotypic Tumor Spheroids. Cancer Discov, 8(2): 196-215.

Jia, Z. & Liang, N. & Li, S. 2020. [Application of Organoids in Lung Cancer Precision Medicine]. Zhongguo Fei Ai Za Zhi, 23(7): 615-620.

John, T., Kohler, D., Pintilie, M., Yanagawa, N., Pham, N. A., Li, M., Panchal, D., Hui, F., Meng, F., Shepherd, F. A., & Tsao, M. S. 2011. The ability to form primary tumor xenografts is predictive of increased risk of   disease recurrence in early-stage non-small cell lung cancer. Clin Cancer Res, 17(1): 134-141.

Kaczmarczyk, J. A., Roberts, R. R., Luke, B. T., Chan, K. C., Van Wagoner, C. M., Felder, R. A., Saul, R. G., Simona, C., & Blonder, J. 2021. Comparative microsomal proteomics of a model lung cancer cell line NCI-H23   reveals distinct differences between molecular profiles of 3D and 2D cultured   cells. Oncotarget, 12(20): 2022-2038.

Kalluri, R. 2016. The biology and function of fibroblasts in cancer. Nat Rev Cancer, 16(9): 582-598.

Kanzaki, M., Yamato, M., Takagi, R., Kikkawa, T., Isaka, T., Okano, T., & Onuki, T. 2013. Controlled collagen crosslinking process in tissue-engineered fibroblast sheets   for preventing scar contracture on the surface of lungs. J Tissue Eng Regen Med, 7(5): 383-391.

Kim, M., Mun, H., Sung, C. O., Cho, E. J., Jeon, H. J., Chun, S. M., Jung, D. J., Shin, T. H., Jeong, G. S., Kim, D. K., Choi, E. K., Jeong, S. Y., Taylor, A. M., Jain, S., Meyerson,

M., & Jang, S. J. 2019. Patient-derived lung cancer organoids as in vitro cancer models for therapeutic   screening. <u>Nat Commun</u>, 10(1): 3991.

Kimbrell, H. Z., Gustafson, K. S., Huang, M., & Ehya, H. 2012. Subclassification of Non-Small Cell Lung Cancer by Cytologic Sampling: A Logical Approach with Selective Use of Immunocytochemistry. <u>Acta Cytologica</u>, 56(4): 419-424.

Koch. 2018. Koch Institut Robert. Krebs in Deutschland für 2017/2018 [Robert Koch Institue. Cancer in Germany (2017/2018)].

Konopleva, M., Martinelli, G., Daver, N., Papayannidis, C., Wei, A., Higgins, B., Ott, M., Mascarenhas, J., & Andreeff, M. 2020. MDM2 inhibition: an important step forward in cancer therapy. <u>Leukemia</u>, 34(11): 2858-2874.

Kropp, B. P. 1998. Small-intestinal submucosa for bladder augmentation: a review of preclinical   studies. <u>World J Urol</u>, 16(4): 262-267.

Kucab, J. E., Hollstein, M., Arlt, V. M., & Phillips, D. H. 2017. Nutlin-3a selects for cells harbouring TP53 mutations. <u>Int J Cancer</u>, 140(4): 877-887.

Kuo, C. H., Lin, M. W., Hsu, Y. W., Chou, H. C., Lin, L. H., Law, C. H., Lin, Y. C., Hu, R. Y., Kuo, W. H., Ko, M. L., Chang, S. J., Lee, Y. R., & Chan, H. L. 2021. Biomarker discovery in highly invasive lung cancer cell through proteomics   approaches. <u>Cell Biochem Funct</u>, 39(3): 367-379.

Kuzet, S. E. & Gaggioli, C. 2016. Fibroblast activation in cancer: when seed fertilizes soil. <u>Cell Tissue Res</u>, 365(3): 607-619.

Lakshmanan, Y., Frimberger, D., Gearhart, J. D., & Gearhart, J. P. 2005. Human embryoid body-derived stem cells in co-culture with bladder smooth muscle   and urothelium. <u>Urology</u>, 65(4): 821-826.

Laurila, R., Parkkila, S., Isola, J., Kallioniemi, A., & Alarmo, E. L. 2013. The expression patterns of gremlin 1 and noggin in normal adult and tumor   tissues. <u>Int J Clin Exp Pathol</u>, 6(7): 1400-1408.

Lilo, M. T., Allison, D., Wang, Y., Ao, M., Gabrielson, E., Geddes, S., Zhang, H., Askin, F., & Li, Q. K. 2016. Expression of P40 and P63 in lung cancers using fine needle aspiration cases.   Understanding clinical pitfalls and limitations. <u>J Am Soc Cytopathol</u>, 5(3): 123-132.

Lin, F., Ren, X. D., Pan, Z., Macri, L., Zong, W. X., Tonnesen, M. G., Rafailovich, M., Bar-Sagi, D., & Clark, R. A. 2011. Fibronectin growth factor-binding domains are required for fibroblast survival. <u>J Invest Dermatol</u>, 131(1): 84-98.

LIN, L., LIN, H., WANG, L., WANG, B., HAO, X., & SHI, Y. 2015. miR-130a regulates macrophage polarization and is associated with non-small cell lung cancer. <u>Oncology Reports</u>, 34(6): 3088-3096.

Liu, S., Zhou, F., Shen, Y., Zhang, Y., Yin, H., Zeng, Y., Liu, J., Yan, Z., & Liu, X. 2016. Fluid shear stress induces epithelial-mesenchymal transition (EMT) in Hep-2 cells. <u>Oncotarget</u>, 7(22): 32876-32892.

Liu, W., Ju, L., Cheng, S., Wang, G., Qian, K., Liu, X., Xiao, Y., & Wang, X. 2020. Conditional reprogramming: Modeling urological cancer and translation to clinics. <u>Clin Transl Med</u>, 10(2): e95.

Liu, X., Ory, V., Chapman, S., Yuan, H., Albanese, C., Kallakury, B., Timofeeva, O. A., Nealon, C., Dakic, A., Simic, V., Haddad, B. R., Rhim, J. S., Dritschilo, A., Riegel, A., McBride, A., & Schlegel, R. 2012. ROCK Inhibitor and Feeder Cells Induce the Conditional Reprogramming of Epithelial Cells. <u>The American Journal of Pathology</u>, 180(2): 599-607.

Lu, S. H., Sacks, M. S., Chung, S. Y., Gloeckner, D. C., Pruchnic, R., Huard, J., de Groat, W. C., & Chancellor, M. B. 2005. Biaxial mechanical properties of muscle-derived cell seeded small intestinal submucosa for bladder wall reconstitution. <u>Biomaterials</u>, 26(4): 443-449.

Lynch, M. D. & Watt, F. M. 2018. Fibroblast heterogeneity: implications for human disease. <u>J Clin Invest</u>, 128(1): 26-35.

Martinez-Outschoorn, U. & Sotgia, F. & Lisanti, M. P. 2014. Tumor microenvironment and metabolic synergy in breast cancers: critical importance of mitochondrial fuels and function. <u>Semin Oncol</u>, 41(2): 195-216.

Martino, M. M. & Hubbell, J. A. 2010a. The 12th-14th type III repeats of fibronectin function as a highly promiscuous growth factor-binding domain. <u>FASEB J</u>, 24(12): 4711-4721.

Martino, M. M. & Hubbell, J. A. 2010b. The 12th-14th type III repeats of fibronectin function as a highly promiscuous growth factor-binding domain. FASEB J, 24(12): 4711-4721.

Matsumoto, T., Holmes, R. H., Burdick, C. O., Heisterkamp, C. R., & O'Connell, T. J. 1966. Replacement of large veins with free inverted segments of small bowel: autografts of submucosal membrane in dogs and clinical use. Ann Surg, 164(5): 845-848.

Nietzer, S., Baur, F., Sieber, S., Hansmann, J., Schwarz, T., Stoffer, C., Häfner, H., Gasser, M., Waaga-Gasser, A. M., Walles, H., & Dandekar, G. 2016a. Mimicking Metastases Including Tumor Stroma: A New Technique to Generate a Three-Dimensional Colorectal Cancer Model Based on a Biological Decellularized Intestinal Scaffold. Tissue Eng Part C Methods, 22(7): 621-635.

Nietzer, S., Baur, F., Sieber, S., Hansmann, J., Schwarz, T., Stoffer, C., Häfner, H., Gasser, M., Waaga-Gasser, A. M., Walles, H., & Dandekar, G. 2016b. Mimicking Metastases Including Tumor Stroma: A New Technique to Generate a Three-Dimensional Colorectal Cancer Model Based on a Biological Decellularized Intestinal Scaffold. Tissue Eng Part C Methods, 22(7): 621-635.

Oskarsson, T., Acharyya, S., Zhang, X. H., Vanharanta, S., Tavazoie, S. F., Morris, P. G., Downey, R. J., Manova-Todorova, K., Brogi, E., & Massagué, J. 2011. Breast cancer cells produce tenascin C as a metastatic niche component to colonize the lungs. Nat Med, 17(7): 867-874.

Pakravan, K., Babashah, S., Sadeghizadeh, M., Mowla, S. J., Mossahebi-Mohammadi, M., Ataei, F., Dana, N., & Javan, M. 2017. MicroRNA-100 shuttled by mesenchymal stem cell-derived exosomes suppresses in vitro angiogenesis through modulating the mTOR/HIF-1α/VEGF signaling axis in breast cancer cells. Cell Oncol (Dordr), 40(5): 457-470.

Pankov, R. & Yamada, K. M. 2002. Fibronectin at a glance. Journal of Cell Science, 115(20): 3861-3863.

Parmaksiz, M. & Elçin, A. E. & Elçin, Y. M. 2018. Decellularization of Bovine Small Intestinal Submucosa. Methods Mol Biol, 1577: 129-138.

Patten, J. & Wang, K. 2021. Fibronectin in development and wound healing. <u>Adv Drug Deliv Rev</u>, 170: 353-368.

Pham, N. A., Radulovich, N., Ibrahimov, E., Martins-Filho, S. N., Li, Q., Pintilie, M., Weiss, J., Raghavan, V., Cabanero, M., Denroche, R. E., Wilson, J. M., Metran-Nascente, C., Borgida, A., Hutchinson, S., Dodd, A., Begora, M., Chadwick, D., Serra, S., Knox, J. J., Gallinger, S., Hedley, D. W., Muthuswamy, L., & Tsao, M. S. 2021. Patient-derived tumor xenograft and organoid models established from resected pancreatic, duodenal and biliary cancers. <u>Sci Rep</u>, 11(1): 10619.

Procopio, M. G., Laszlo, C., Al, L. D., Kim, D. E., Bordignon, P., Jo, S. H., Goruppi, S., Menietti, E., Ostano, P., Ala, U., Provero, P., Hoetzenecker, W., Neel, V., Kilarski, W. W., Swartz, M. A., Brisken, C., Lefort, K., & Dotto, G. P. 2015. Combined CSL and p53 downregulation promotes cancer-associated fibroblast activation. <u>Nat Cell Biol</u>, 17(9): 1193-1204.

Quatromoni, J. G. & Eruslanov, E. 2012. Tumor-associated macrophages: function, phenotype, and link to prognosis in human lung cancer. <u>Am J Transl Res</u>, 4(4): 376-389.

Rashtbar, M., Hadjati, J., Ai, J., Jahanzad, I., Azami, M., Shirian, S., Ebrahimi-Barough, S., & Sadroddiny, E. 2018. Characterization of decellularized ovine small intestine submucosal layer as extracellular matrix-based scaffold for tissue engineering. <u>J Biomed Mater Res B Appl Biomater</u>, 106(3): 933-944.

Recasens, A. & Munoz, L. 2019. Targeting Cancer Cell Dormancy. <u>Trends Pharmacol Sci</u>, 40(2): 128-141.

Rekhtman, N., Ang, D. C., Sima, C. S., Travis, W. D., & Moreira, A. L. 2011. Immunohistochemical algorithm for differentiation of lung adenocarcinoma and squamous cell carcinoma based on large series of whole-tissue sections with validation in small specimens. <u>Mod Pathol</u>, 24(10): 1348-1359.

Roy, A. & Bera, S. 2016. CAF cellular glycolysis: linking cancer cells with the microenvironment. <u>Tumour Biol</u>, 37(7): 8503-8514.

Sachs, N., Papaspyropoulos, A., Zomer-van, O. D., Heo, I., Böttinger, L., Klay, D., Weeber, F., Huelsz-Prince, G., Iakobachvili, N., Amatngalim, G. D., de Ligt, J., van

Hoeck, A., Proost, N., Viveen, M. C., Lyubimova, A., Teeven, L., Derakhshan, S., Korving, J., Begthel, H., Dekkers, J. F., Kumawat, K., Ramos, E., van Oosterhout, M. F., Offerhaus, G. J., Wiener, D. J., Olimpio, E. P., Dijkstra, K. K., Smit, E. F., van der Linden, M., Jaksani, S., van de Ven, M., Jonkers, J., Rios, A. C., Voest, E. E., van Moorsel, C. H., van der Ent, C. K., Cuppen, E., van Oudenaarden, A., Coenjaerts, F. E., Meyaard, L., Bont, L. J., Peters, P. J., Tans, S. J., van Zon, J. S., Boj, S. F., Vries, R. G., Beekman, J. M., & Clevers, H. 2019. Long-term expanding human airway organoids for disease modeling. EMBO J, 38(4).

Sack, K. D. & Teran, M. & Nugent, M. A. 2016. Extracellular Matrix Stiffness Controls VEGF Signaling and Processing in Endothelial Cells. J Cell Physiol, 231(9): 2026-2039.

Schütte, M., Risch, T., Abdavi-Azar, N., Boehnke, K., Schumacher, D., Keil, M., Yildiriman, R., Jandrasits, C., Borodina, T., Amstislavskiy, V., Worth, C. L., Schweiger, C., Liebs, S., Lange, M., Warnatz, H. J., Butcher, L. M., Barrett, J. E., Sultan, M., Wierling, C., Golob-Schwarzl, N., Lax, S., Uranitsch, S., Becker, M., Welte, Y., Regan, J. L., Silvestrov, M., Kehler, I., Fusi, A., Kessler, T., Herwig, R., Landegren, U., Wienke, D., Nilsson, M., Velasco, J. A., Garin-Chesa, P., Reinhard, C., Beck, S., Schäfer, R., Regenbrecht, C. R., Henderson, D., Lange, B., Haybaeck, J., Keilholz, U., Hoffmann, J., Lehrach, H., & Yaspo, M. L. 2017. Molecular dissection of colorectal cancer in pre-clinical models identifies biomarkers predicting sensitivity to EGFR inhibitors. Nat Commun, 8: 14262.

Schweinlin, M., Rossi, A., Lodes, N., Lotz, C., Hackenberg, S., Steinke, M., Walles, H., & Groeber, F. 2017. Human barrier models for the in vitro assessment of drug delivery. Drug Delivery and Translational Research, 7(2): 217-227.

Shamir, E. R. & Ewald, A. J. 2014. Three-dimensional organotypic culture: experimental models of mammalian biology and disease. Nature Reviews Molecular Cell Biology, 15(10): 647-664.

Shen, Y., Xiang, Y., Huang, X., Zhang, Y., & Yue, Z. 2022. Pharmacogenomic Cluster Analysis of Lung Cancer Cell Lines Provides Insights into Preclinical Model Selection in NSCLC. Interdiscip Sci, 14(3): 712-721.

Shi, R., Radulovich, N., Ng, C., Liu, N., Notsuda, H., Cabanero, M., Martins-Filho, S. N., Raghavan, V., Li, Q., Mer, A. S., Rosen, J. C., Li, M., Wang, Y., Tamblyn, L., Pham, N., Haibe-Kains, B., Liu, G., Moghal, N., & Tsao, M. 2020. Organoid Cultures as Preclinical Models of Non–Small Cell Lung Cancer. Clinical Cancer Research, 26(5): 1162-1174.

Siolas, D. & Hannon, G. J. 2013. Patient-derived tumor xenografts: transforming clinical samples into mouse   models. Cancer Res, 73(17): 5315-5319.

Sos, M. L., Michel, K., Zander, T., Weiss, J., Frommolt, P., Peifer, M., Li, D., Ullrich, R., Koker, M., Fischer, F., Shimamura, T., Rauh, D., Mermel, C., Fischer, S., Stückrath, I., Heynck, S., Beroukhim, R., Lin, W., Winckler, W., Shah, K., LaFramboise, T., Moriarty, W. F., Hanna, M., Tolosi, L., Rahnenführer, J., Verhaak, R., Chiang, D., Getz, G., Hellmich, M., Wolf, J., Girard, L., Peyton, M., Weir, B. A., Chen, T. H., Greulich, H., Barretina, J., Shapiro, G. I., Garraway, L. A., Gazdar, A. F., Minna, J. D., Meyerson, M., Wong, K. K., & Thomas, R. K. 2009. Predicting drug susceptibility of non-small cell lung cancers based on genetic   lesions. J Clin Invest, 119(6): 1727-1740.

Spada, S., Tocci, A., Di Modugno, F., & Nisticò, P. 2021. Fibronectin as a multiregulatory molecule crucial in tumor matrisome: from structural and functional features to clinical practice in oncology. Journal of Experimental & Clinical Cancer Research, 40(1): 102.

Syed, O., Walters, N. J., Day, R. M., Kim, H. W., & Knowles, J. C. 2014. Evaluation of decellularization protocols for production of tubular small   intestine submucosa scaffolds for use in oesophageal tissue engineering. Acta Biomater, 10(12): 5043-5054.

Tan, Q., Liu, R., Chen, X., Wu, J., Pan, Y., Lu, S., Weder, W., & Luo, Q. 2017. Clinic application of tissue engineered bronchus for lung cancer treatment. J Thorac Dis, 9(1): 22-29.

ter Horst, E. N., Hakimzadeh, N., van der Laan, A. M., Krijnen, P. A., Niessen, H. W., & Piek, J. J. 2015. Modulators of Macrophage Polarization Influence Healing of the Infarcted   Myocardium. Int J Mol Sci, 16(12): 29583-29591.

Terra, M., Oberkampf, M., Fayolle, C., Rosenbaum, P., Guillerey, C., Dadaglio, G., & Leclerc, C. 2018. Tumor-Derived TGFβ Alters the Ability of Plasmacytoid Dendritic Cells to Respond to Innate Immune Signaling. <u>Cancer Res</u>, 78(11): 3014-3026.

Totonelli, G., Maghsoudlou, P., Garriboli, M., Riegler, J., Orlando, G., Burns, A. J., Sebire, N. J., Smith, V. V., Fishman, J. M., Ghionzoli, M., Turmaine, M., Birchall, M. A., Atala, A., Soker, S., Lythgoe, M. F., Seifalian, A., Pierro, A., Eaton, S., & De Coppi, P. 2012. A rat decellularized small bowel scaffold that preserves villus-crypt architecture for intestinal regeneration. <u>Biomaterials</u>, 33(12): 3401-3410.

Travis, W. D., Brambilla, E., Noguchi, M., Nicholson, A. G., Geisinger, K., Yatabe, Y., Ishikawa, Y., Wistuba, I., Flieder, D. B., Franklin, W., Gazdar, A., Hasleton, P. S., Henderson, D. W., Kerr, K. M., Petersen, I., Roggli, V., Thunnissen, E., & Tsao, M. 2013. Diagnosis of Lung Cancer in Small Biopsies and Cytology: Implications of the 2011 International Association for the Study of Lung Cancer/American Thoracic Society/European Respiratory Society Classification. <u>Archives of Pathology & Laboratory Medicine</u>, 137(5): 668-684.

Tsai, H., Yang, K., Wu, M., Chen, J., & Tseng, C. 2019. The Effects of Different Dynamic Culture Systems on Cell Proliferation and Osteogenic Differentiation in Human Mesenchymal Stem Cells. <u>International Journal of Molecular Sciences</u>, 20(16): 4024.

VanSlyke, J. K. & Boswell, B. A. & Musil, L. S. 2018. Fibronectin regulates growth factor signaling and cell differentiation in primary lens cells. <u>J Cell Sci</u>, 131(22).

Voloshenyuk, T. G., Landesman, E. S., Khoutorova, E., Hart, A. D., & Gardner, J. D. 2011. Induction of cardiac fibroblast lysyl oxidase by TGF-β1 requires PI3K/Akt, Smad3, and MAPK signaling. <u>Cytokine</u>, 55(1): 90-97.

Wang, D., Pham, N. A., Tong, J., Sakashita, S., Allo, G., Kim, L., Yanagawa, N., Raghavan, V., Wei, Y., To, C., Trinh, Q. M., Starmans, M. H., Chan-Seng-Yue, M. A., Chadwick, D., Li, L., Zhu, C. Q., Liu, N., Li, M., Lee, S., Ignatchenko, V., Strumpf, D., Taylor, P., Moghal, N., Liu, G., Boutros, P. C., Kislinger, T., Pintilie, M., Jurisica, I., Shepherd, F. A., McPherson, J. D., Muthuswamy, L., Moran, M. F., & Tsao, M. S. 2017. Molecular heterogeneity of non-small cell lung carcinoma patient-derived xenografts closely reflect their primary tumors. <u>Int J Cancer</u>, 140(3): 662-673.

Wang, L., Zhao, Y., Yang, F., Feng, M., Zhao, Y., Chen, X., Mi, J., Yao, Y., Guan, D., Xiao, Z., Chen, B., & Dai, J. 2020. Biomimetic collagen biomaterial induces in situ lung regeneration by forming   functional alveolar. Biomaterials, 236: 119825.

Weeber, F., Ooft, S. N., Dijkstra, K. K., & Voest, E. E. 2017. Tumor Organoids as a Pre-clinical Cancer Model for Drug Discovery. Cell Chem Biol, 24(9): 1092-1100.

Wu, F. & Wang, L. & Zhou, C. 2021. Lung cancer in China: current and prospect. Curr Opin Oncol, 33(1): 40-46.

Yan, M., Sun, L., Li, J., Yu, H., Lin, H., Yu, T., Zhao, F., Zhu, M., Liu, L., Geng, Q., Kong, H., Pan, H., & Yao, M. 2019. RNA-binding protein KHSRP promotes tumor growth and metastasis in non-small cell   lung cancer. J Exp Clin Cancer Res, 38(1): 478.

Yatabe, Y., Dacic, S., Borczuk, A. C., Warth, A., Russell, P. A., Lantuejoul, S., Beasley, M. B., Thunnissen, E., Pelosi, G., Rekhtman, N., Bubendorf, L., Mino-Kenudson, M., Yoshida, A., Geisinger, K. R., Noguchi, M., Chirieac, L. R., Bolting, J., Chung, J. H., Chou, T. Y., Chen, G., Poleri, C., Lopez-Rios, F., Papotti, M., Sholl, L. M., Roden, A. C., Travis, W. D., Hirsch, F. R., Kerr, K. M., Tsao, M. S., Nicholson, A. G., Wistuba, I., & Moreira, A. L. 2019. Best Practices Recommendations for Diagnostic Immunohistochemistry in Lung   Cancer. J Thorac Oncol, 14(3): 377-407.

Zakowski, M. F., Rekhtman, N., Auger, M., Booth, C. N., Crothers, B., Ghofrani, M., Khalbuss, W., Laucirica, R., Moriarty, A. T., Tabatabai, Z. L., & Barkan, G. A. 2016. Morphologic Accuracy in Differentiating Primary Lung Adenocarcinoma From Squamous Cell Carcinoma in Cytology Specimens. Archives of Pathology & Laboratory Medicine, 140(10): 1116-1120.

Zhang, Y., Lin, H. K., Frimberger, D., Epstein, R. B., & Kropp, B. P. 2005. Growth of bone marrow stromal cells on small intestinal submucosa: an alternative   cell source for tissue engineered bladder. BJU Int, 96(7): 1120-1125.

Zhang, Z., Wang, H., Ding, Q., Xing, Y., Xu, Z., Lu, C., Luo, D., Xu, L., Xia, W., Zhou, C., & Shi, M. 2018. Establishment of patient-derived tumor spheroids for non-small cell lung cancer. PLOS ONE, 13(3): e194016.

Zhao, X., Qu, J., Sun, Y., Wang, J., Liu, X., Wang, F., Zhang, H., Wang, W., Ma, X., Gao, X., & Zhang, S. 2017. Prognostic significance of tumor-associated macrophages in breast cancer: a   meta-analysis of the literature. Oncotarget, 8(18): 30576-30586.

Zheng, R. S., Sun, K. X., Zhang, S. W., Zeng, H. M., Zou, X. N., Chen, R., Gu, X. Y., Wei, W. W., & He, J. 2019. [Report of cancer epidemiology in China, 2015]. Zhonghua Zhong Liu Za Zhi, 41(1): 19-28.

9. Acknowledgement

10.   Sworn declaration

I hereby declare that I did produce the doctoral dissertation submitted to the Faculty of Medicine of Otto von Guericke University entitled

ESTABLISHMENT OF A THREE-DIMENSIONAL (3D) LUNG CANCER

MODEL FOR TRANSLATIONAL RESEARCH

in the Magdeburg University hospital

with support from University Clinic for Cardiac and Thoracic Surgery.

without any other assistance and that I did not use any other resources in the writing of the dissertation than those listed here.

No rights of third parties were infringed in the writing of this dissertation.

I have not previously submitted this dissertation to any domestic or foreign university.

I hereby confer upon the Faculty of Medicine the right to produce and distribute additional copies of my dissertation.

Magdeburg,

Signature

11.   Declaration of Criminal Convictions Template

I hereby declare that I have not been convicted of a criminal offense with an academic connection.

Magdeburg,

Signature

12. Education background and publications

Education Background

2011-2016 Bachelor degree of medicine in Binzhou Medicine University

2016-2019 Master degree of medicine in Binzhou Medicine University

Resident doctor in Binzhou Medicine University Hospital

2021- Doctoral study in Magdeburg University

Previous scientific achievements

Meeting presentation

This work was presented at the 30th Annual Meeting of the European Society of Thoracic Surgeons in The Hague, June 21st 2022.

Hailong Wang, Thorsten Walles, Cornelia Wiese-Rischke. Patient-derived lung cancer ″sandwich cultures″ with preserved tumor microenvironment. Tissue Engineering. Submitted.